Supplementary Information (SI) for Journal of Materials Chemistry A.
This journal is © The Royal Society of Chemistry 2025

Supplementary information for

Weaving strength and conductivity: spider silk-modulated polymer electrolytes for high-performance all-solid-state lithium-metal batteries

Cheng-Hao Liao,[a] Ming-Yan Shen,[b] Yi-Jen Wang,[b] Tsung-Yu Yu,[a] Ru-Jong Jeng,[a] Ta-I Yang,[c] Matthew B. Dickerson,[d] Chia-Suei Hung,[d] Jeremy S. Knopp,[e] Hsuan-Chen Wu,[b,*] Shih-Huang Tung [a,f,*]

[a] Institute of Polymer Science and Engineering, National Taiwan University, Taipei 10617, Taiwan
[b] Department of Biochemical Science and Technology, National Taiwan University, Taipei 10617, Taiwan
[c] Department of Chemical Engineering, Chung Yuan Christian University, Taoyuan 32023, Taiwan
[d] Air Force Research Laboratory, WPAFB, Ohio 45433, USA
[e] Armatus Inc., Tokyo 1051701, Japan
[f] Department of Materials Science and Engineering, National Taiwan University, Taipei 10617, Taiwan

*Corresponding authors.
Email addresses: hcwu7@ntu.edu.tw (H.-C. Wu), shtung@ntu.edu.tw (S.-H. Tung)

S1. Experimental section

S1.1. Materials

Chemicals and reagents. Polyethylene oxide (PEO, M_n = 400,000 g mol^{-1}), 1,1,1,3,3,3-hexafluoro-2-propanol (HFIP), and bis(trifluoromethane) sulfonimide lithium salt (LiTFSI, 99.0 %) were purchased from Sigma-Aldrich. PEO and HFIP were stored in a dry box, and the LiTFSI was stored in an argon-filled glove box that was maintained at < 0.1 ppm O_2 and H_2O. CR2032 coin cell components (cases, springs, and stainless-steel spacers) were purchased from UBIQ Technology Co., Ltd. 2-mil thick Kapton tape was purchased from Tape Masters. Sodium nitrate ($NaNO_3$, 99.5 %), graphite (<20 μm), potassium permanganate ($KMnO_4$, 99.0 %), hydrogen peroxide solution (H_2O_2, 30 %), and hydrochloric acid (HCl, 37 %) were all sourced from Sigma-Aldrich. Concentrated sulfuric acid (H_2SO_4, 98 %) was obtained from J.T. Baker. All chemicals and items were used as received unless otherwise stated.

Silk materials. The native spider silk collection followed the procedure previously reported.[1] In brief, female *Nephila pilipes* were gently secured on polystyrene foam plates. Major ampullate (MA) dragline silks were directly extracted from the spinnerets of immobilized spiders using a motorized rotor under a dissecting microscope. The silk was collected at a reeling speed of approximately 0.5 - 1 m min^{-1}. The collected spider silk samples were then stored for further experiments.

For collecting silkworm silk, *Bombyx mori* cocoons underwent a degumming process involving treatment with 0.02 M Na_2CO_3 at 80 °C for 1 hour. Following this, the cocoons were rinsed, dried, and dissolved in 9.3M LiBr at 60 °C for 4 hours. The solution was then dialyzed in deionized water and lyophilized to obtain silk fibroin powder for subsequent usage.[2]

The bioengineered spider silk materials (R1 and R2) were synthesized and prepared following the procedure reported in our previous paper.[3] Both spider silk proteins consist of a repetitive domain flanked by the N-terminal domain (NTD) and C-terminal domains (CTD) derived from *Nephila* spiders. The core repetitive region of R1, MaSp1 origin, is designed with the sequence GAGAAAAAASGAGQGGYGRQGGQTS, repeated 32 times. In contrast, the repetitive region of R2, derived from MaSp2, follows the sequence GPGGYGPGQQGPSGPAAAAAAGPGG-YGPGQQTS, also with 32 repetitions. Both R1 and R2 genes were constructed in pET28 vectors and subsequently transformed into *E. coli* BLR(DE3) Δ*endA* strain for further bioproduction.

Following expression, the spider silk proteins underwent SDS purification and were lyophilized for storage and experiments.

S1.2. Sample preparation

Preparation of blend films. The blend films were fabricated using the solvent casting technique. First, PEO was dissolved in HFIP to generate a PEO solution. Bioengineered R1 or R2 was then introduced into the PEO solution in varying mass ratios (10%, 25%, 50%, 75%, and 90%). After dissolving for one day, the mixture solution was spread onto a polytetrafluoroethylene (PTFE) Petri dish for casting. The film was allowed to dry at room temperature for one day and was subsequently stored in a vacuum desiccator until further use.

Preparation of solid electrolytes. The SPE films were fabricated using the solvent casting method. First, the specified amount of LiTFSI was dispersed in HFIP by sonication. Subsequently, R2 with different mass ratios (10%, 15%, 20%, 25%, and 35%) was introduced to LiTFSI solution. Once R2 was completely dissolved, PEO was incorporated into the solution. The molar ratio of [EO]:[Li] was maintained at 15:1. Note that LiTFSI is insoluble in HFIP alone; however, PEO and R2 can facilitate its dissolution in HFIP due to their intermolecular interactions. After thorough stirring to achieve a homogeneous mixture, the solution was poured onto a PTFE Petri dish, dried at 25 °C for 48 hours, and vacuum-dried at 60 °C for 24 hours to ensure complete solvent evaporation. This process resulted in the formation of SPE films with an approximate thickness of 200 μm. These electrolyte films were further maintained in an argon-filled glove box with O_2 and H_2O content below 0.1 ppm for an additional 24 hours. Finally, the prepared SPE films were cut into 18 mm diameter disks for subsequent testing and characterization.

Preparation of $LiFePO_4$ cathode. The slurry of $LiFePO_4$, Super P carbon, and polyvinylidene fluoride (PVDF) at a ratio of 80:10:10 was prepared using N-methyl-2-pyrrolidone (NMP) as a solvent. This mixture was thoroughly homogenized and then uniformly cast onto aluminum foil. The aluminum foil was immediately dried at 70 °C to remove excess solvent, followed by further drying in a vacuum oven at 80 °C for 24 hours to ensure complete solvent evaporation. The $LiFePO_4$ composite cathode was stored in an argon-filled glove box. The final thickness of the dry cathodes was approximately 0.1 mm, with a mass load about 2 - 3 mg cm^{-2}.

Coin cell preparation. Samples were prepared within CR2032 coin cells within an Ar glove box to ensure an inert environment. All components of the coin cells, made from stainless steel, were sourced from UBIQ Technology Co., Ltd. The preparation of the samples involved layering SPE between stainless steel discs with Kapton tape utilized as a spacer. Coin cell components for evaluating ionic conductivity were arranged in the following order: bottom case, disc, SPE sample, disc, spring, and top case. For plating and stripping tests, the assembly sequence was adjusted to: bottom case, disc, lithium sheet, SPE sample, lithium sheet, disc, spring, and top case. Similarly, coin cell components for assessing cycling performance were organized in the following sequence: bottom case, disc, $LiFePO_4$ cathode, SPE sample, metallic lithium, disc, spring, and top case. To seal the coin cell, a UBIQ Technology Co., Ltd. C2000-A crimper was employed.

S1.3. Characterization

^{13}C cross-polarization magic-angle-spinning nuclear magnetic resonance spectroscopy (^{13}C CP/MAS NMR). NMR spectra were acquired on a wide-bore 14.1-T Bruker Advance III spectrometer. Larmor frequencies for ^{1}H, ^{13}C and ^{15}N are 600.21, 150.92 and 60.82 MHz, respectively. ^{13}C CP/MAS NMR spectra were acquired with a 2.5 mm magic-angle-spinning (MAS) double-resonance probe head with a sample spinning rate of 21 kHz. The contact time for the cross-polarization (CP) scheme was set to 2 ms. The ^{1}H TPPM decoupling with the radio-frequency field strength of 100 kHz was utilized during the acquisition, with the recycle delay at 3 s.

Attenuated total reflection Fourier transform infrared spectroscopy (ATR-FTIR). IR spectra were obtained with a JASCO FT/IR-4600 spectrometer equipped with an ATR PRO450-S sampling module. All measurements were conducted in an ambient environment (25 °C), scanning from 500 cm^{-1} to 4000 cm^{-1}, with a total of 32 scans performed for each sample. To ensure optimal contact and accurate readings, the samples were securely clamped onto the diamond ATR crystal during the measurement process.

Small-angle/wide-angle X-ray scattering (SAXS/WAXS). The characteristics of samples related to microstructures were examined through small-angle X-ray scattering (SAXS) and wide-angle X-ray scattering (WAXS) measurements on BL23A beamline in the National Synchrotron

Radiation Research Center (NSRRC), Taiwan. All samples were prepared in an argon-filled glove box and sealed in 9 cm diameter Petri dishes, which were then stored in a desiccator to prevent moisture absorption. Scattering of samples were recorded under ambient conditions with a 5-minute exposure time. The resultant 2D diffraction data was analyzed using XSACT software to obtain plots of scattering intensity versus scattering vector q.

One-dimensional (1-D) correlation function $\Gamma(z)$. 1-D correlation function $\Gamma(z)$ analysis from the SAX data was performed by the SasView software, where z is the length of real space. $\Gamma(z)$ describes the spatial correlation by the similarity of electron density and structure of two different positions in an arbitrary direction,[4] expressed as

$$\Gamma(z) = \frac{1}{Q_0}\int_0^\infty I(q)q^2\cos(qz)\,dq \quad (1)$$

where $I(q)$ is the scattering intensity of the sample. Q_0 is the invariant given by

$$Q_0 = \int_0^\infty I(q)q^2 dq \quad (2)$$

The maximum value of $\Gamma(z)$ is 1, occurring at the origin due to self-correlation. To derive $\Gamma(z)$ from the SAXS data, the original data were first extrapolated to $q = 0$ and $q = \infty$ using the Guinier and Porod laws, respectively. The combined data, including the original and the Guinier/Porod extrapolations, were then transformed into $\Gamma(z)$ using Eq. (1). In this study, $\Gamma(z)$ is interpreted based on an ideal two-phase lamellar system, consisting of periodic crystalline and amorphous phases. From this model, structural parameters including the long period (L_p), the sum of the crystalline phase thickness (L_c) and the amorphous phase thickness (L_a), can be directly extracted. The position of the second maximum in the 1-D correlation function profile represents L_p. L_c is determined by the intersection of the extended straight line along the initial descending curve with the horizontal tangent at the first minimum. L_a is then calculated by $L_p - L_c$.

X-ray photoelectron spectroscopy (XPS). Hard X-ray photoelectron spectroscopy (HAXPES) was used to determine the elemental compositions of the protein samples, conducted on a ULVAC-PHI instrument. The setup was equipped with a dual-scanning X-ray source, with Cr Kα X-ray (5.4 KeV) and Al Kα X-ray (1.4 KeV). The binding energy scale was calibrated to 284.3 eV based on the prominent C 1s peak.

Tensile testing. The tensile tests of the samples were conducted on a universal testing machine (JSV-H1000) at a tensile rate of 10 mm min^{-1} at ambient temperature (25 °C) and relative humidity of 66%. All tensile specimens were cut into the shape of dog bones for the tensile tests. The thickness and width of the tensile specimens were 0.5 mm and 5 mm, respectively. The length of the sample specimens between the two manual grippers of the tensile testing machine was 20 mm.

Thermogravimetric analysis (TGA). The thermal stability of the samples was investigated using a TA Instruments Q50. The analysis was conducted at a heating rate of 10 °C min^{-1} in a nitrogen atmosphere.

Differential scanning calorimetry (DSC). DSC measurements were conducted using a TA Instruments Discovery DSC 25. Samples weighing between 5 and 8 mg were enclosed in aluminum pans within a glovebox. Experiments were performed using a heat-cool-heat profile with temperatures ranging from −80 °C to 200 °C at a heating rate of 10 °C min^{-1}. The glass transition temperature (T_g) for each sample was determined from the analysis of the second heating curves, employing the midpoint at half-height method for accurate extraction. The PEO crystallinity χ_c of samples is calculated by

$$\chi_c = \frac{\Delta H_m}{f_{PEO}\Delta H_{PEO}} \times 100\% \quad (3)$$

where ΔH_m is the enthalpy of the melting, and ΔH_{PEO} is the ideal melting enthalpy of 100% crystallization of PEO, which is 203 J g^{-1}. f_{PEO} is the PEO weight fraction in the sample.

Rheology. Rheology measurements were performed using a TA Instruments DHR-2 rheometer. Samples were pressed into a disk inside an argon-filled glove box and then loaded onto the rheometer. The measurements were conducted using an 8 mm parallel plate and a consistent sample thickness of approximately 1 mm was maintained across all measurements. A series of frequency sweeps, ranging from 10 to 0.01 Hz, were conducted. The procedure involved initially heating the samples from 30 °C to 100 °C, followed by cooling back down to 30 °C. Measurements were taken at every 10 °C interval while applying a strain of 0.1%. To ensure that the material reached an equilibrium state, all samples were held at the specified temperature for at least 1 hour prior to initiating the frequency sweep.

Scanning electron microscopy (SEM). SEM images were taken on a JOEL JSM-6700F at an accelerating voltage of 10 keV. Specimens were sputtered with platinum prior to imaging.

Polarized optical microscopy (**POM).** POM analysis was conducted using the OLYMPUS BX53M equipped with LINKAM heating stage and charge-coupled device (CCD) camera. The specimens were sandwiched between two glass slides.

Adhesion test. The adhesion strength of SPEs was measured using a force gauge (MET-DFG5). All samples were prepared as 1 cm^2 squares and sandwiched between two identical substrates. The lap shear testing was employed at a constant tensile speed of 20 mm min^{-1}, with the maximum force recorded. Adhesion strength was calculated by dividing the maximum force by the contact area. All measurements were conducted in a glove box filled with Ar (O_2 < 0.1 ppm, H_2O < 0.1 ppm).

S1.4. Electrochemical measurements

Ionic conductivity. The electrochemical impedance spectrum was measured using the Biologic SP-50e electrochemical workstation, applying an oscillation voltage of 10 mV over a frequency range of 1 MHz to 1 Hz and at temperatures ranging from 30 °C to 80 °C. The electrolyte film was positioned between two stainless steel blocking electrodes, each with a diameter of 16 mm. To enhance the accuracy of the measurements and reduce interfacial impedance between the electrolyte and the stainless-steel cathodes, the assembled SS|SPE|SS cell was activated at 80 °C for 48 hours prior to testing. Additionally, samples were allowed to stabilize at each test temperature for at least 2 hours before recording the impedance response. The collected data were subsequently used to calculate the ionic conductivity by the following equation:

$$\sigma = \frac{L}{R \times S} \tag{4}$$

where L represents the thickness of the electrolyte film, R denotes the resistance of the bulk electrolyte, and S indicates the contact area between the electrode and the electrolyte. The activation energy E_a corresponding to the change of ionic conductivity with temperature was determined using the Arrhenius equation.

Linear sweep voltammetry (LSV). The electrochemical stability windows (ESW) were studied by LSV on Biologic SP-50e electrochemical workstation. The LSV test was conducted over a voltage range of 3.0 to 6.0 V (vs. Li^+/Li) with a scanning rate of 1 mV s^{-1} to examine the electrochemical stability of the electrolytes at 80 °C. The SS|SPE|Li battery assemblies were prepared within an argon glove box.

Transference number. Li^+ transference numbers for different SPEs were determined by combining AC impedance and DC polarization measurements at 60 °C, using a symmetric battery with a Li metal diameter of 15 mm at a voltage of 10 mV. The symmetric battery was subjected to DC polarization at this voltage. The following equation was utilized to calculate the transference number:

$$t_{\mathrm{Li}}^{+} = \frac{I_{\mathrm{S}}(\Delta V - I_0 R_0)}{I_0(\Delta V - I_{\mathrm{S}} R_{\mathrm{S}})} \quad (5)$$

where I_0 and I_S represent the initial and steady-state currents flowing through the battery, respectively. R_0 and R_S denote the resistance values before and after polarization, respectively, obtained from the impedance spectrum of the battery in the frequency range of 1 MHz to 0.1 Hz, with an oscillating voltage of 10 mV.

Charge-discharge performance of lithium-ion batteries. All-solid-state lithium-ion batteries (2032 type) were assembled in an argon-filled glove box, maintaining oxygen and moisture levels below 0.1 ppm. $LiFePO_4$ was utilized as the cathode, while metallic lithium served as the anode. The charge and discharge performance of $LiFePO_4$|SPE|Li batteries was carried out using a battery testing system (Neware CT-4008) across a voltage range of 2.5 to 4.0 V at a temperature of 60 °C and 25 °C. Prior to cycle testing, the batteries were heated for 24 hours to activate and improve the interface between the electrodes and the electrolyte. This heating process not only enhanced contact but also resulted in a reduction of interfacial resistance between the electrodes and the electrolytes.

S2. Supplementary data

S2.1. NMR characterization of bioengineered spider silks

Solid-state ^{13}C CP/MAS NMR was used to probe spider silk protein conformations in crystalline and amorphous phases. **Table S1** summarizes band assignments from the typical ^{13}C CP/MAS NMR spectrum of both R1 and R2 (**Fig. 3b**). In the aliphatic area, ^{13}C CP/MAS NMR detected Gly Cα (43.4 ppm), Gln Cα (55.4 ppm), Cβ (26.4 ppm), and Cγ (31.1 ppm); Ser Cα (53.1 ppm) and Cβ (61.7 ppm); Pro Cα (62.4 ppm), Cβ (30.4 ppm), Cγ (24.0 ppm), and Cδ (50.0 ppm). Aromatic carbons mainly arise from Tyr C1 (129.5 ppm), C2,6 (130.9 ppm), C3,5 (115.6 ppm), and C4 (156.1 ppm). Carbonyl carbons in peptide bonds lie between 172.3 and 176.3 ppm and merge into one major peak centered at 173.0 ppm. Chemical shifts were used to identify the secondary structure, with Ala Cα resonating at 54.7 ppm for helix structures and at 49.8 ppm for β-sheet structures.

The peaks within the aliphatic carbon region for R1 display significantly higher signal intensity. The higher signal intensity of peaks associated with β-sheets, primarily from polyalanine (Cβ at 21.2 ppm and Cα at 49.8 ppm), indicates that the R1 protein has greater crystallinity than R2. In contrast, the β-sheet peak intensity in the aliphatic carbon region of R2 is lower. The Ala Cβ peak at 16.6 ppm and Tyr Cα peak at 61.6 ppm, indicative of β-turn and helix structure, respectively, suggests R2 is more flexible than R1. This aligns with the protein sequences: (GA)n/An sequence promotes a rigid β-sheet structure, especially in R1, while GPGQQ, GPGGX, and GGX sequences of R2 favor β-turn/spiral and helix formations that enhance flexibility.

Table S1. ^{13}C chemical shifts of the main amino acid residues for R1 and R2 materials.

Residues	^{13}C	$\delta^{13}C$ [ppm] (measured)	$\delta^{13}C$ [ppm] (reference)	Ref.
Alanine (Ala)	Cα (α-helix)	54.7	54.4-56.4	5-8
	Cα (β-sheet)	49.8	49.6-52.1	
	Cβ (β-turn)	16.6	~17.0	
	Cβ (β-sheet)	21.2	19.3-23.1	
Clycine (Gly)	Cα (random coil)	43.4	43.5-45.3	5,6,8
Glutamine (Gln)	Cα	55.4	55.0-55.3	5,7
	Cβ	26.4	26.5	

	Cγ	31.1	31.7-32.0	
Serine (Ser)	Cα	53.1	~53.0	5-7,9
	Cβ	61.7	61.4-62.1	
Tyrosine (Tyr)	Cα (α-helix)	61.6	60.2-62.2	5,6,10
	Cα (β-sheet)	55.8	55.4-57.9	
	Cβ (β-sheet)	43.1	39.1-42.9	
	Aromatic C	129.5 [C1]	129.0 [C1]	
		130.9 [C2,6]	131.4 [C2,6]	
		115.6 [C3,5]	116.3 [C3,5]	
		156.1 [C4]	155.9 [C4]	
Proline (Pro)	Cα	62.4	~62.0	7,8
	Cβ	30.4	~30.0	
	Cγ	24.0	~24.0	
	Cδ	50.0	~50.0	

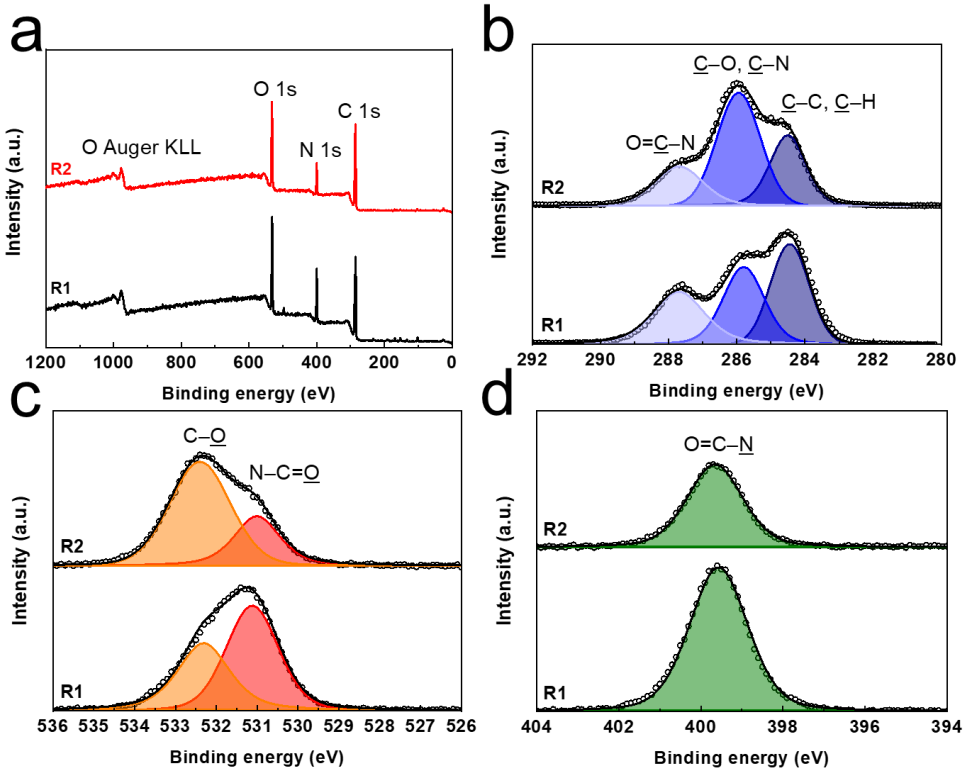

Fig. S1. Elemental analysis of bioengineered spidroins. (a) Full XPS spectra, (b) C 1s spectra, (c) O 1s spectra, and (d) N 1s spectra of R1 and R2 spidroins with deconvoluted bands.

S2.2. Elemental composition analysis of bioengineered spider silks by XPS

Elemental composition analysis of the bioengineered spider silks (R1 and R2) was conducted using X-ray photoelectron spectroscopy (XPS). **Fig. S1a** depicts typical survey results for R1 and R2, with detected photoelectrons from O 1s, N 1s, and C 1s and no residual elements. Deconvoluted XPS spectra for C 1s, O 1s, and N 1s are presented in **Fig. S1b** to **S1d**, respectively. **Table S2** and **Table S3** summarize the high-resolution scan analysis for R1 and R2. O 1s, N 1s, and C 1s are observed at binding energies around 530, 399, and 285 eV,[11,12] respectively, with elemental compositions matching theoretical estimates. Multiple chemical states were resolved using Gaussian-Lorentzian deconvolution. For R2, the C 1s peak deconvolutes into three peaks at 284.5, 285.8, and 287.7 eV, corresponding to C–C/C–H, C–O/C–N, and O=C–N groups. The atomic percentages align with theoretical values, confirming measurement accuracy. R2 exhibits relatively higher C 1s signal of C–O/C–N at 285.8 eV and O 1s signal of C–O at 532.4 eV than R1, consistent with the protein sequences where R2 contains more proline and tyrosine residues that contribute to increased C–N and C–O content.

Table S2. XPS data for R1 protein.

Elements	Elemental composition (%)	Components	Binding energy (eV)	Functional composition (%)
C	48.57	C–C, C–H	284.5	18.29
		C–N, C–O	285.9	15.99
		O=C–N	287.7	14.29
N	16.57	O=C–N	399.6	16.57
O	34.85	N–C=O	531.0	20.46
		C–O	532.3	14.39

Table S3. XPS data for R2 protein.

Elements	Elemental composition (%)	Components	Binding energy (eV)	Functional composition (%)
C	50.33	C–C, C–H	284.5	14.24
		C–N, C–O	285.8	25.46
		O=C–N	287.7	10.63
N	11.11	O=C–N	399.6	11.11
O	38.56	N–C=O	531.1	11.20
		C–O	532.4	27.36

S2.3. Molecular characterization of bioengineered spider silks by FTIR

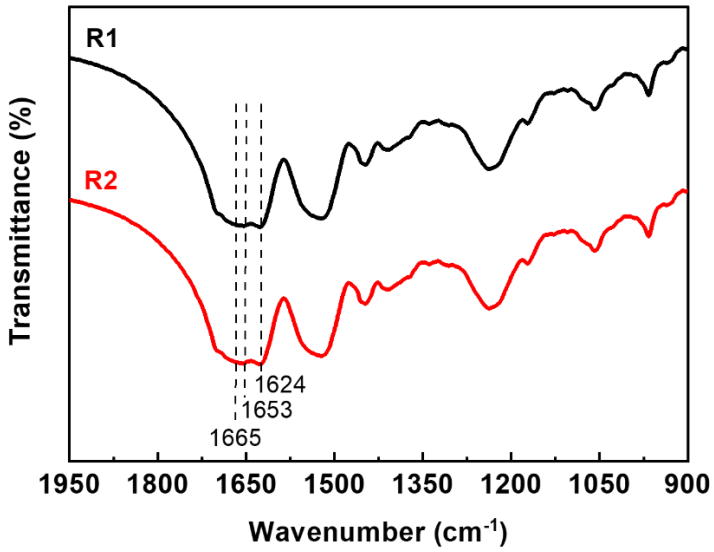

Fig. S2. ATR-IR spectra of the bioengineered spider silks, R1 and R2.

Fig. S2 presents the ATR-FTIR spectra of the bioengineered spider silk materials, R1 and R2, with **Table S4** summarizing the corresponding band assignments. The analysis reveals important vibrational characteristics of the bioengineered silks, providing insights into their molecular structure. The spectrum features the amide I band, which spans the range of 1590–1700 cm^{-1} and is primarily attributed to C=O stretching. Notable peaks at 1624 cm^{-1}, 1653 cm^{-1}, and 1665 cm^{-1} indicate the presence of β-sheet, random coil/helix, and β-turn structures, respectively. Additionally, the amide II band is observed between 1460–1590 cm^{-1}, corresponding to C–N stretching vibrations, while the amide III band, found in the 1200–1400 cm^{-1} range, is associated with N–H bending and stretching. Both R1 and R2 exhibited typical absorption peaks corresponding to their own functional groups, confirming structural characteristics.

Table S4. Absorption bands of ATR-FTIR for R1 and R2.

Wavenumber [cm^{-1}] (measured)	Wavenumber (reference)	Assignment	Ref.
966	963	Ala (CH_3 rock, N−Cα stretch)	5,13,14
	1055	Ala (Cα–Cβ stretch)	13
1063	1065	CH_3 rock, C−N stretch	15

1171	1164–1170	Tyr (C−N stretch), Ala (Hα bend, CH_3 symmetric bend)	13,15
1238	1230–1240	Amide III (random coil and α-helical)	13,15-17
	1260–1270	Amide III (β-sheet)	15,17
1337	1315–1350	CH bend	15,18
1411	1410	Gln (C−N stretch)	18
1447	1425–1480	Ala (CH_2 bend, CH_3 asymmetric bend)	15,18
1520	1510–1520	Amide II (β-sheet)	15,19
1535	1535–1542	Amide II (random coil and α-helical)	17,19
1624	1610–1630	Amide I (β-sheet)	15,17,19
1653	1648–1660	Amide I (random coil and α-helical)	
1665	1665	Amide I (β-turn and bend)	20

S2.4. Structural analysis of bioengineered spider silks via WAXS

WAXS was used to investigate the crystalline structure of bioengineered spider silk, revealing that R1 has a higher crystallinity than R2. The WAXS pattern (**Fig. S3**) shows a main diffraction peak at q = 1.4 Å^{-1}, with shoulders at 1.2 and 1.7 Å^{-1}, corresponding to (120), (200), and (211) planes, respectively.[21,22] These crystalline diffractions are possibly attributed to the ordered structure of the β-sheet.[23] Furthermore, the crystallinity could be estimated according to the following equation:

$$\chi(\%) = \frac{A_c}{A_c + A_a} \times 100\% \quad (6)$$

where A_a and A_c are the total areas of diffractions for the amorphous region and the crystalline region, respectively. The calculated crystallinity is 55.8% for R1 and 45.5% for R2, respectively. This estimated crystallinity is similar to that of natural spider silk dragline.[24,25] The higher crystallinity of R1 aligns with its $(GA)_n/A_n$-rich sequence promoting β-sheet formation, while R2, with GPGQQ and GPGGX, forms β-spirals, resulting in more flexible properties.

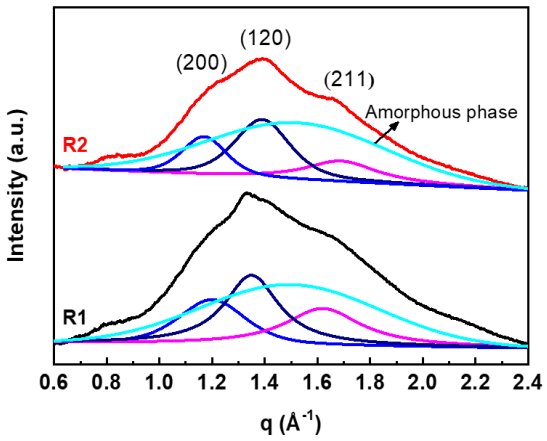

Fig. S3. WAXS data with deconvoluted peaks for bioengineered spider silks, R1 and R2.

S2.5. Bioengineered spider silk in tunning the tensile performance of PEO

The incorporation of bioengineered spider silk into PEO significantly enhances the mechanical properties, as demonstrated through tensile testing (**Fig. 2c** and **2d**), with further corresponding quantitative results depicted in **Fig. S4** and **S5**. In **Fig. S4**, the results indicate that PEO/R1 blends containing varying proportions of R1 show a marked increase in tensile strength, elongation, and toughness compared to neat PEO. Specifically, the tensile strength of the PEO/R1 blends increases from 8.8 MPa for neat PEO to 55.3 MPa for P/R1-40. Furthermore, a maximum elongation at break of 576.8% is observed at a 10% R1, and it decreases to 155.2% when the R1 content reaches 30%. The P/R1-15 blend exhibits the highest toughness of 151.2 MJ m^{-3} – 5 times greater than that of neat PEO, which underscores the potential of R1 as an effective modifier for enhancing mechanical performance.

In contrast, while PEO/R2 blends (**Fig. S5**), exhibited slightly lower tensile strength compared to PEO/R1 blends, their elongation at break and toughness are significantly higher. Similarly, as the proportion of R2 in the PEO blends increases, the tensile strength of the PEO/R2 blends exhibits an upward trend. Notably, when the weight percentage of R2 reaches 25%, the blend exhibits the highest elongation at break of 1196.9% and the highest toughness of 248.7 MJ m^{-3}. This difference is attributed to the unique flexibility of R2, which contains motifs such as GPGQQ and GPGGX that contribute to higher ductility. Overall, tensile testing provides critical insights into the strength, flexibility, and ductility of these PEO/silk blends, validating the hypothesis that the mechanical properties could be finely tuned by adjusting the ratios of bioengineered spider silk. These findings highlight the effectiveness of spider silk in enhancing the robustness of PEO for applications.

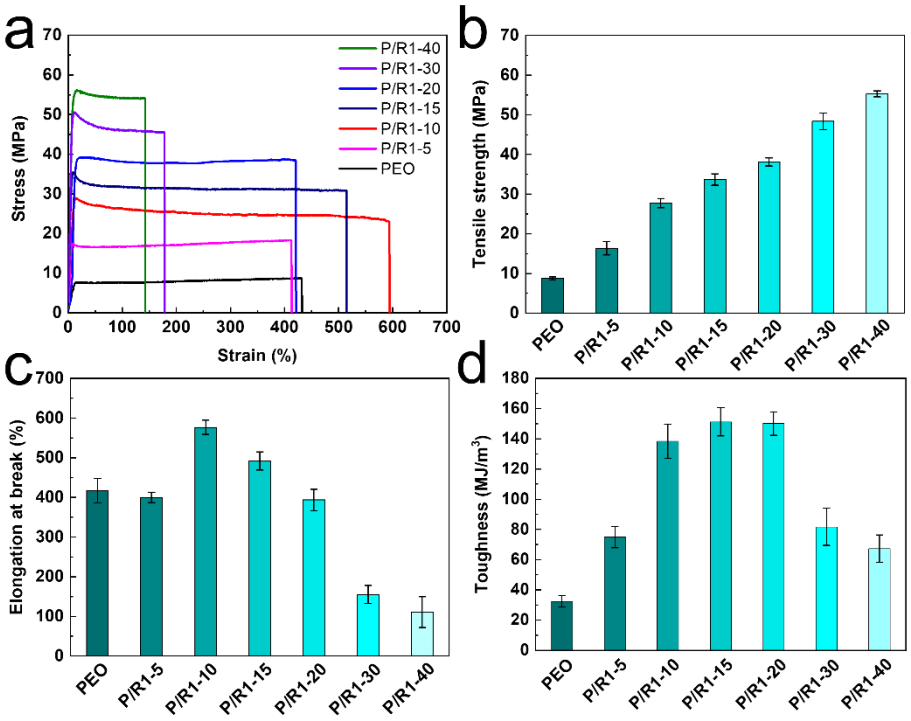

Fig. S4. Impact of R1 on the mechanical performance of PEO: (a) Stress-strain curves of PEO/R1 blends, (b) tensile strength, (c) elongation at break, and (d) toughness obtained from (a). The error bars were calculated by performing at least three replicates for each blend.

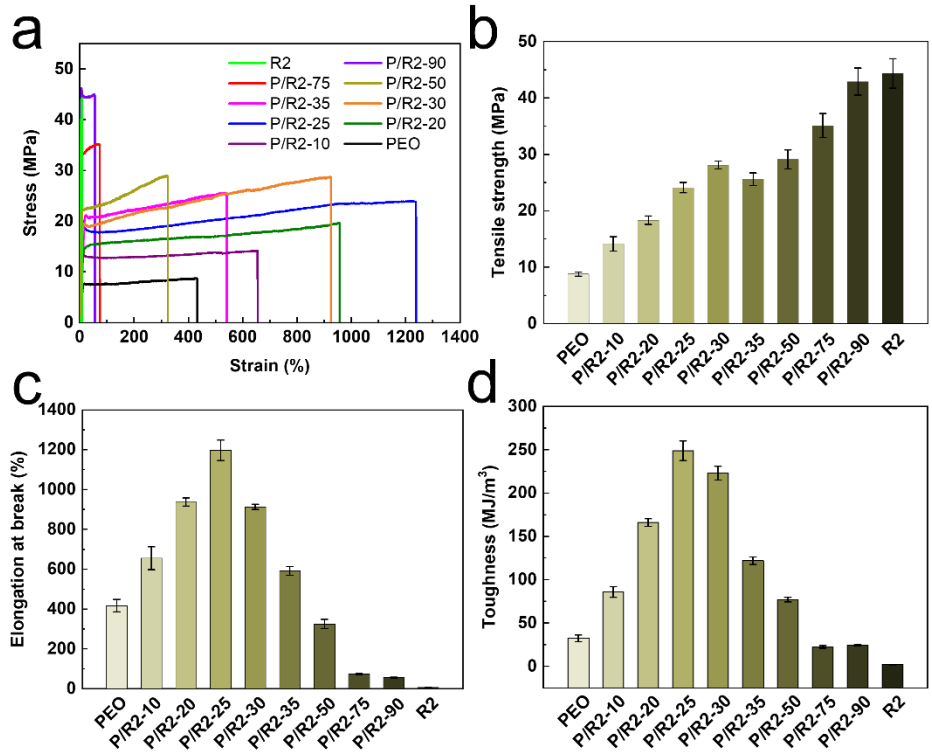

Fig. S5. Impact of R2 on the mechanical performance of PEO: (a) Stress-strain curves of PEO/R2 blends, (b) tensile strength, (c) elongation at break, and (d) toughness obtained from (a). The error bars were calculated by performing at least three replicates for each blend.

S2.6. Effects of R2 on the melting behaviors of PEO

The DSC data of the PEO/R2 blends are shown in **Fig. S6**. The melting enthalpy of 203 J g^{-1} for 100% crystallinity of PEO is utilized in the calculation of crystallinity χ_c. The melting point T_m and crystallinity χ_c of neat PEO are 70.6 °C and 89.0%, respectively. Addition of R2 lowers T_m and χ_c of PEO, as listed in **Table S5**. T_m decreases to 63.5 °C and χ_c decreases to 31.5% as R2 fraction increases to 80%. Note that the χ_c values of the blends are modified by the PEO fraction. The reduction in T_m of PEO indicates that R2 is a compatible impurity for PEO. Furthermore, the suppression of PEO crystallinity caused by R2 generally implies that there are intermolecular interactions between PEO and R2, which hinders the diffusion and nucleation of PEO chains.

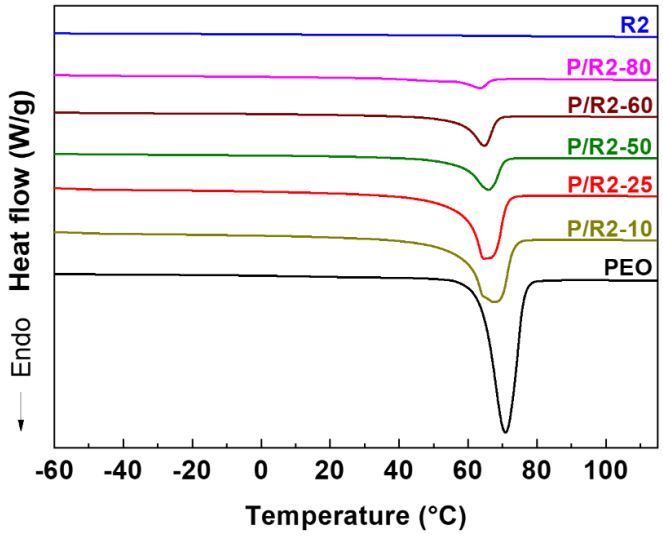

Fig. S6. DSC thermograms of PEO/R2 blends with varying R2 weight fraction.

Table S5. Melting behaviors of PEO in PEO/R2 blends obtained from **Fig. S6**.

Sample	T_m (°C)	ΔH_m (J/g)	χ_c (%)
P/R2-80	63.5	12.8	31.5
P/R2-60	64.7	33.8	41.6
P/R2-50	65.9	43.5	43.9
P/R2-25	66.4	95.8	62.9
P/R2-10	67.6	120.5	66.0
PEO	70.9	180.8	89.0

S2.7. Alteration of the crystal lamellar structure of PEO by bioengineered spider silks

The crystal structures of PEO blended with various bioengineered spider silks (R1 and R2) were investigated through SAXS measurements. As indicated in **Fig. 4a**, SAXS profiles of PEO/R2 blends at different weight percentages show a primary scattering peak and higher-order peaks at positions of a 1:2:3 ratio, indicating the crystalline lamellar structure of PEO. Similarly, PEO/R1 blends display a comparable SAXS pattern, as seen in **Fig. S7**, indicating that R1 also possesses a high degree of miscibility with PEO. The scattering peaks are less pronounced and eventually discernible as the R1 content increases. This could be attributed to a reduction in the crystallinity of PEO, due to the ability of R1 to effectively inhibit and constrain the formation of PEO crystallites.

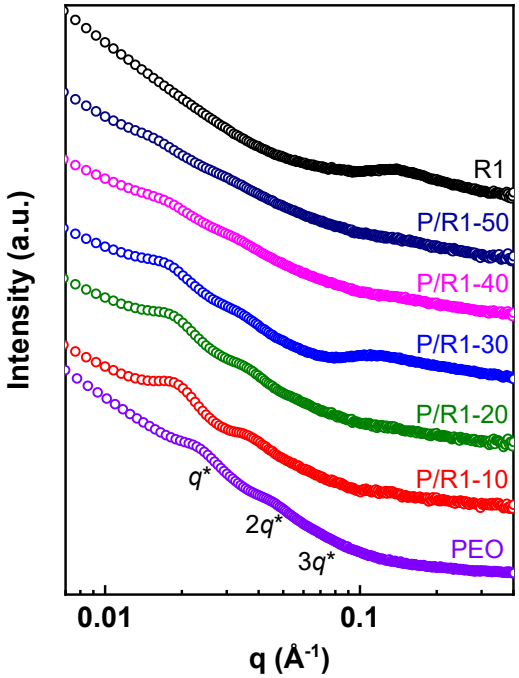

Fig. S7. SAXS profiles of PEO/R1 blends with different R1 fractions.

In addition to SAXS measurements, the crystal lamellar structures within the PEO blends were analyzed using the one-dimensional correlation function, $\Gamma(z)$, obtained from the SAXS profiles. **Fig. S8** presents the one-dimensional electron density correlation function profiles for the PEO/R2 blends. This analysis confirms the presence of lamellar structures and provides quantitative measures of structural changes induced by R2. Specifically, the function is used to calculate the

long-period values L_p, which represents the sum of the lamellar thickness L_c and the thickness of the amorphous layers L_a, as listed in **Table S6** and illustrated in **Fig. 4b**.

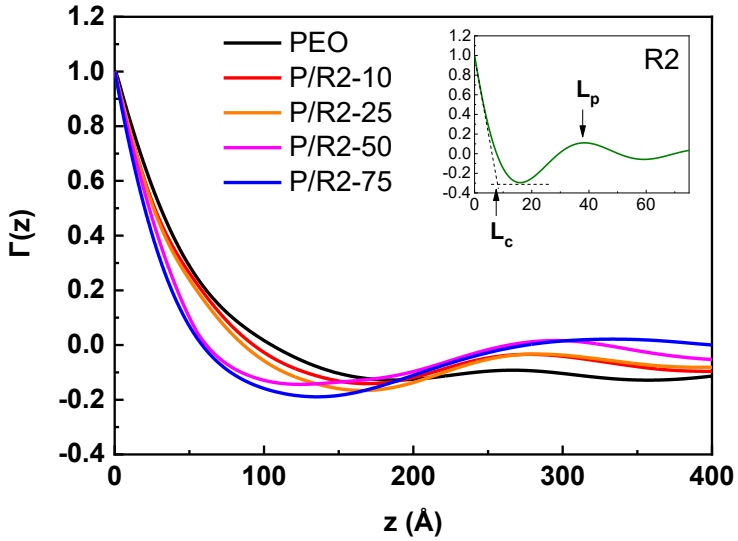

Fig. S8. One-dimensional correlation functions of PEO/R2 blends derived from the SAXS data in **Fig. 4a**.

Table S6. Structural parameters of PEO crystal lamellae extracted from **Fig. S8**.

Sample	L_c (nm)	L_a (nm)	L_p (nm)
P/R2-75	3.3	29.1	32.4
P/R2-50	4.1	25.4	29.5
P/R2-25	5.3	23.0	28.3
P/R2-10	6.1	21.3	27.4
PEO	6.7	19.9	26.6

S2.8. Change in morphology of PEO induced by R2

Fig. S9 illustrates the crystalline behavior of PEO films and the morphological changes induced by the addition of R2 through the observation of polarized optical microscopy (POM). The neat PEO film exhibits clear large spherulites, a feature of regular radial growth of lamellae from the limited nucleation sites. Blending with R2 reduces the sizes of the spherulites, indicating

that R2 can work as nucleating agent and promote the nucleation of PEO. The fact that the spherulites remain impinging on one another and become coarsening upon blending implies that R2 is embedded between lamellae within the spherulites. At 90% R2, the crystal domains disappear, leading to a uniform film. The results suggest that R2 is compatible with PEO, effectively disrupting crystal domains and enhancing the amorphous phase in the blends.

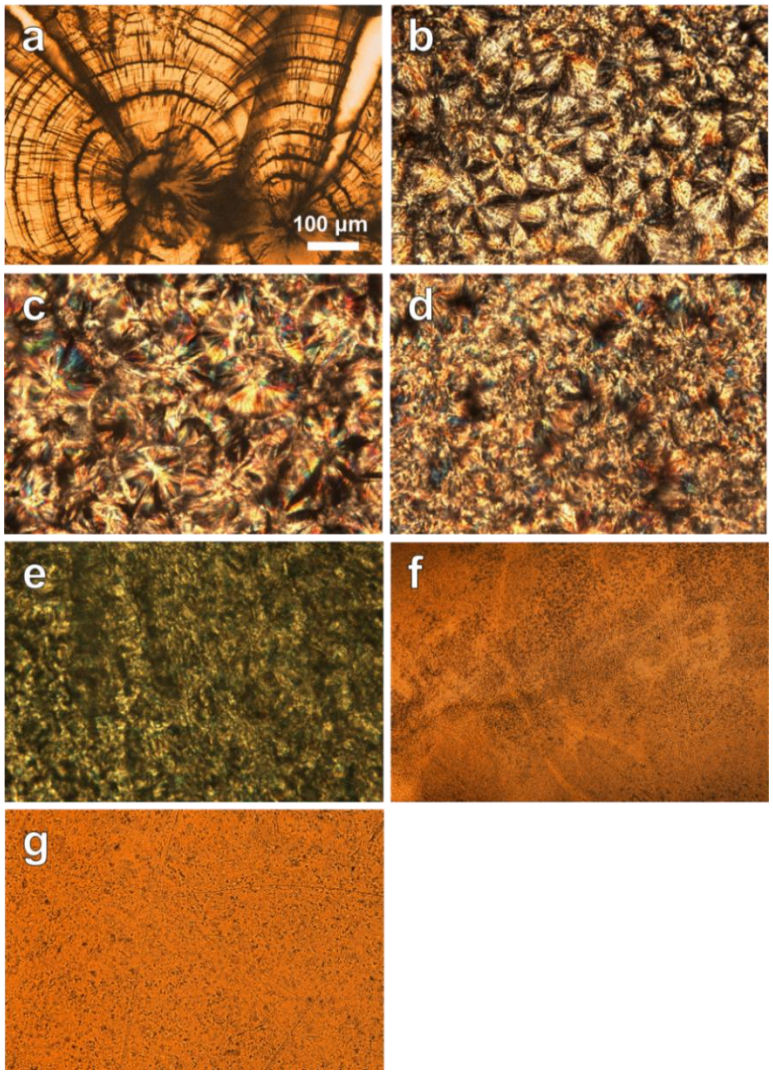

Fig. S9. POM images of PEO/R2 blends: (a) pure PEO, (b) P/R2-10, (c) P/R2-25, (d) P/R2-50, (e) P/R2-75, (f) P/R2-90, and (g) pure R2.

Additionally, morphological analysis of PEO was also performed via SEM. As shown in **Fig. S10**, spherulites of PEO are clearly visible, originating from nucleation sites and spreading in a ripple-like pattern until they contact each other and form boundaries. Adding 10% R2 reduces the spherulite size from approximately 0.3 mm to 0.03 mm, as R2 provides nucleation sites for PEO.

As R2 ratio increases to 25% and 50%, the spherical morphology becomes less distinct, transitioning to irregular strip-shaped structures. At 75% R2, PEO spherulites nearly disappear, leaving a V-shaped valley-like crystalline structure. With 90% R2, the PEO crystal vanishes entirely, resulting in a smooth and flat surface. Pure R2 displays a completely flat and smooth surface.

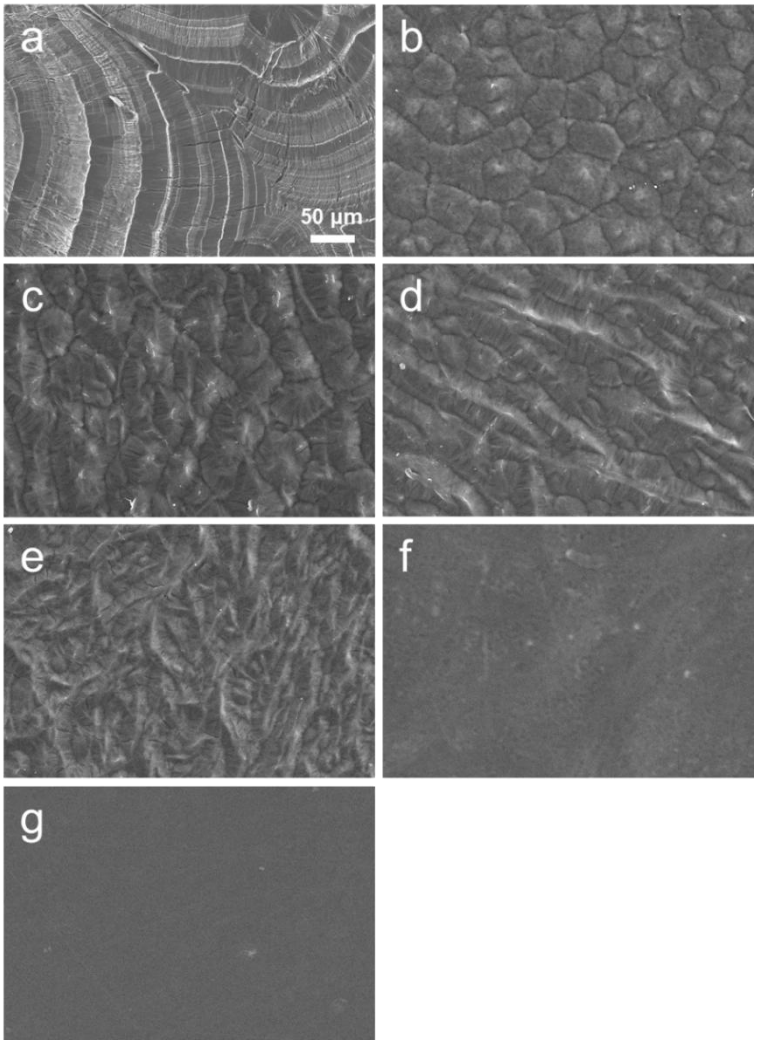

Fig. S10. SEM images of PEO/R2 blends: ((a) pure PEO, (b) P/R2-10, (c) P/R2-25, (d) P/R2-50, (e) P/R2-75, (f) P/R2-90, and (g) pure R2.

S2.9. Evaluation of intermolecular interaction in PEO/R2 blends

Attenuated total reflectance-Fourier transform infrared (ATR-FTIR) spectroscopy was utilized to explore the miscibility and interaction between R2 and PEO. As depicted in **Fig. S11**,

the ATR-FTIR spectra reveal the characteristic absorption peaks of R2 and PEO. A key observation is the slight shift of the C–O–C stretching band of PEO from 1110 cm^{-1} to 1088 cm^{-1} in the PEO/R2 blends. This shift to lower frequencies indicates increased hydrogen bonding between the C–O–C groups of PEO and the N–H groups of R2.[26,27] The formation of hydrogen bonds results in the withdrawal of lone pair electrons on the oxygen atom of C–O–C groups by the hydrogen atom of N–H groups, thus reducing the electron density on the C–O bond and leading to the redshift in the C–O–C stretching.[28,29] The enhanced hydrogen bonding is a compelling explanation for the observed improvements in mechanical properties when PEO is blended with R2. Furthermore, this interaction provides insight into how R2 interferes with the crystallization of PEO. The increased hydrogen bonding suppresses the ability of PEO chains to diffuse and nucleate, thereby hindering crystallization and expanding amorphous phases. This understanding is crucial for tailoring PEO blends for applications that require specific structures and mechanical properties.

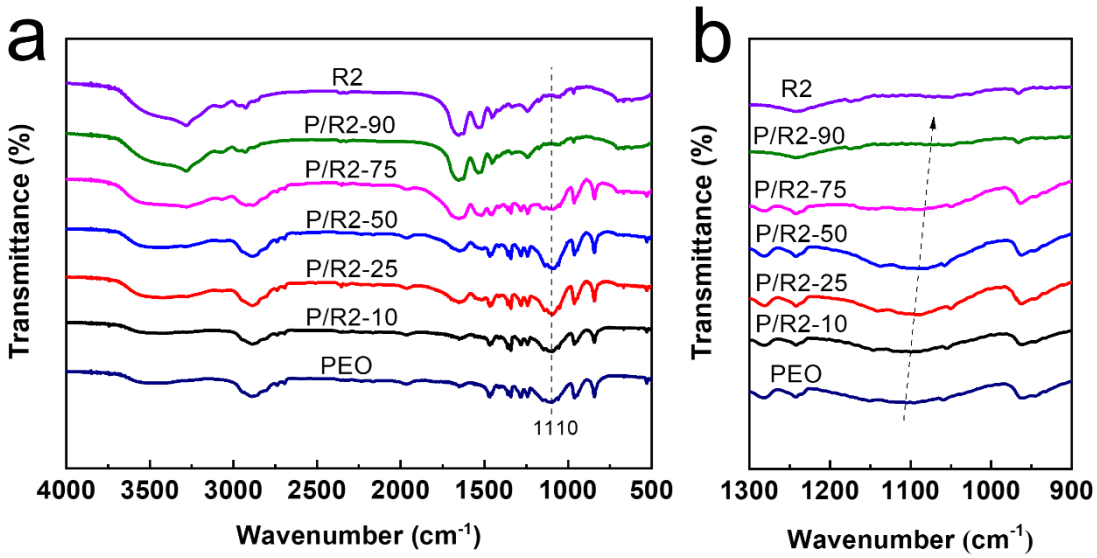

Fig. S11. ATR-FTIR data of PEO/R2 blends: (a) Full spectra and (b) shift around 1110 cm^{-1}.

S2.10. Thermal stabilities of PEO/spidroin blends

Thermogravimetric analysis (TGA) reveals the impact of bioengineered spider silk proteins (R1 and R2) on PEO thermal stability (**Fig. S12** and **S13**). The pure R2 curve shows four distinct weight loss stages from 100 °C to 800 °C. The first two observed stages, between 160 °C – 250 °C and 250 °C – 370 °C, are attributed to peptide bond cleavage and side chain group degradation.

The third and four stages, from 370 °C to 800 °C, involves β-sheet structure breakdown. Pure PEO exhibits thermal decomposition between 300 °C and 440 °C, with the most substantial mass loss occurring near 400 °C. In comparison, pure PEO exhibits a T_{d5} (5% weight loss temperature) of 359 °C, significantly higher than that of pure R1 (259 °C) and R2 (197 °C). In PEO/R1 and PEO/R2 blends, the thermal stability of composites increases with increasing PEO content (**Fig. S14**). Notably, adding just 10% PEO to R2 raises the T_{d5} from 197 °C to 265.4 °C, indicating the compatibility between PEO and R2 and their synergistic effects on enhancing the overall thermal stability of the blends. Additionally, these blends exhibit excellent resistance to thermal decomposition, making them suitable for applications that require high thermal performance alongside enhanced mechanical properties.

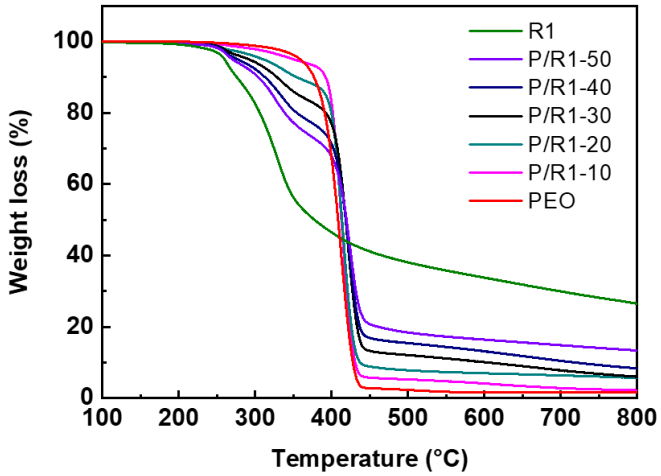

Fig. S12. TGA curves of the PEO/R1 blends.

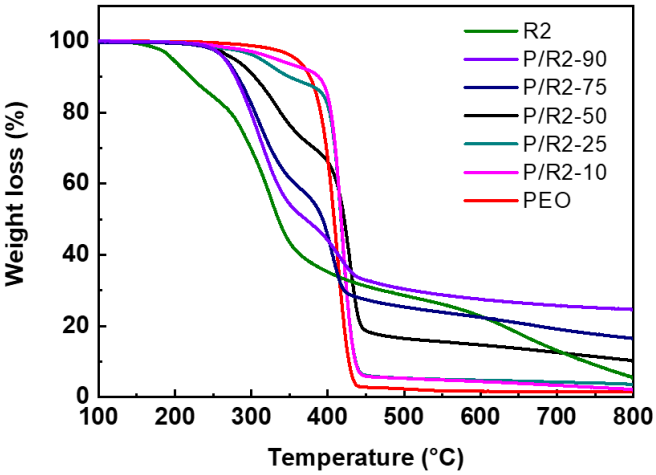

Fig. S13. TGA curves of the PEO/R2 blends.

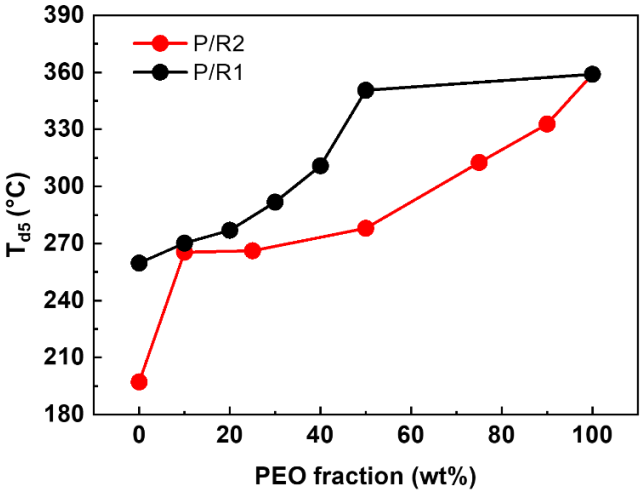

Fig. S14. T_{d5} changes with PEO fraction for PEO/R1 and PEO/R2 blends.

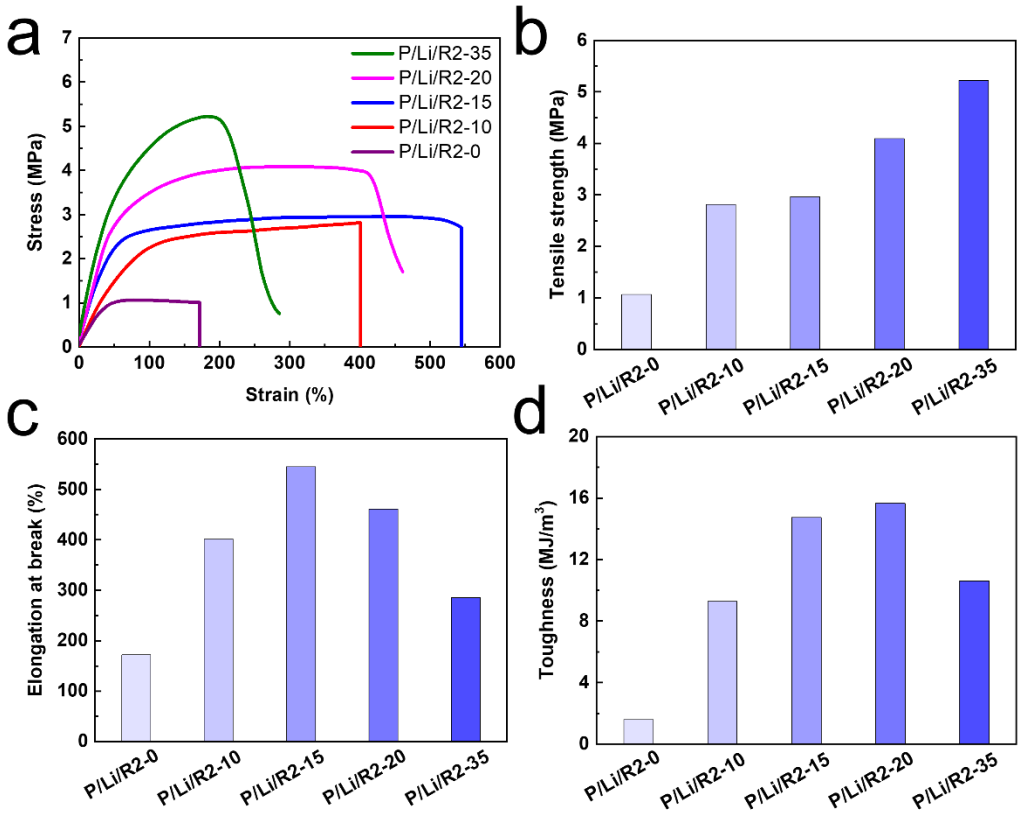

Fig. S15. Tensile performance of PEO/LiTFSI/R2 SPEs. (a) Stress-strain curves of PEO-based SPEs with varying R2 content, (b) tensile strength, (c) elongation, and (d) toughness derived from the stress-strain curves in (a).

S2.11. Mechanical properties of PEO-based SPEs enhanced by R2

In **Fig. S15**, the tensile testing results highlight the enhanced mechanical properties of PEO-based SPEs with the reinforcement of R2. Pure PEO exhibits 417.3% elongation, 8.8 MPa tensile

strength, and 32.4 MJ m^{-3} toughness (**Fig. S4**). The addition of LiTFSI to PEO significantly reduced its mechanical performance. The PEO/LiTFSI SPE without R2 (P/Li/R2-0) shows an elongation at break of 171.8%, a tensile strength of 1.1 MPa, and a toughness of 1.6 MJ m^{-3}. This reduction is due to the decreased crystallinity of PEO as the Li^+ ions coordinate with the polymer matrix. Incorporating R2 into the PEO/LiTFSI SPE notably enhances mechanical performance. The tensile strength monotonically increases with R2 content, the elongation at break peaks at 544.7% for P/Li/R2-15, and the toughness reaches the maximum at 15.7 MJ m^{-3} for P/Li/R2-20. Overall, the superior mechanical properties of the R2-modified SPEs are crucial for ASSLMBs applications.

S2.12. Rheological properties of PEO/LiTFSI/R2 SPEs

The dynamic rheological analyses of SPEs for the evaluation of the viscoelastic behaviors were performed. The addition of R2 to PEO-based SPEs increases the storage modulus (G') and enhances the mechanical properties, aligning with tensile testing results (**Fig. S15**). In **Fig. S16**, the rheological behaviors of the PEO/LiTFSI SPE without R2 (P/Li/R2-0) across temperatures ranging from 30 °C to 100 °C are demonstrated. Notably, a crossover point occurred at 60 °C, where G' equals to the loss modulus (G''). The inverse of the crossover frequency represents the relaxation time of the polymer chains. When G' exceeds G'', the material exhibits an elastic behavior; when G' is lower than G'', it shows a viscous behavior. For P/Li/R2-0, the crossover occurs at 0.01 Hz at 60 °C, with a slight shift from 0.01 Hz to 0.03 Hz as temperature increases, suggesting a more liquid-like behavior due to enhanced PEO chain mobility at elevated temperature.

In **Fig. S17,** the rheological data of P/Li/R2-20 SPE, conducted at temperature range of 30 °C to 100 °C, show no crossover between G' and G'' across the 0.01 Hz to 10 Hz frequency. This indicates that R2 imparts elasticity to the SPEs despite the reduction of PEO crystallinity, displaying a favorable characteristic of a successful SPE to battery performance. Strong mechanical properties assist in preventing lithium dendrite formation during charging and discharging. Ion transport in SPEs relies on the PEO amorphous region, where the EO units associate with lithium ions and exhibit chain flexibility for rapid ion transport. Therefore, minimizing PEO crystallinity is essential for an efficient ion movement. Consequently, PEO/LiTFSI/R2 SPEs show significant promise for practical applications in ASSLMBs.

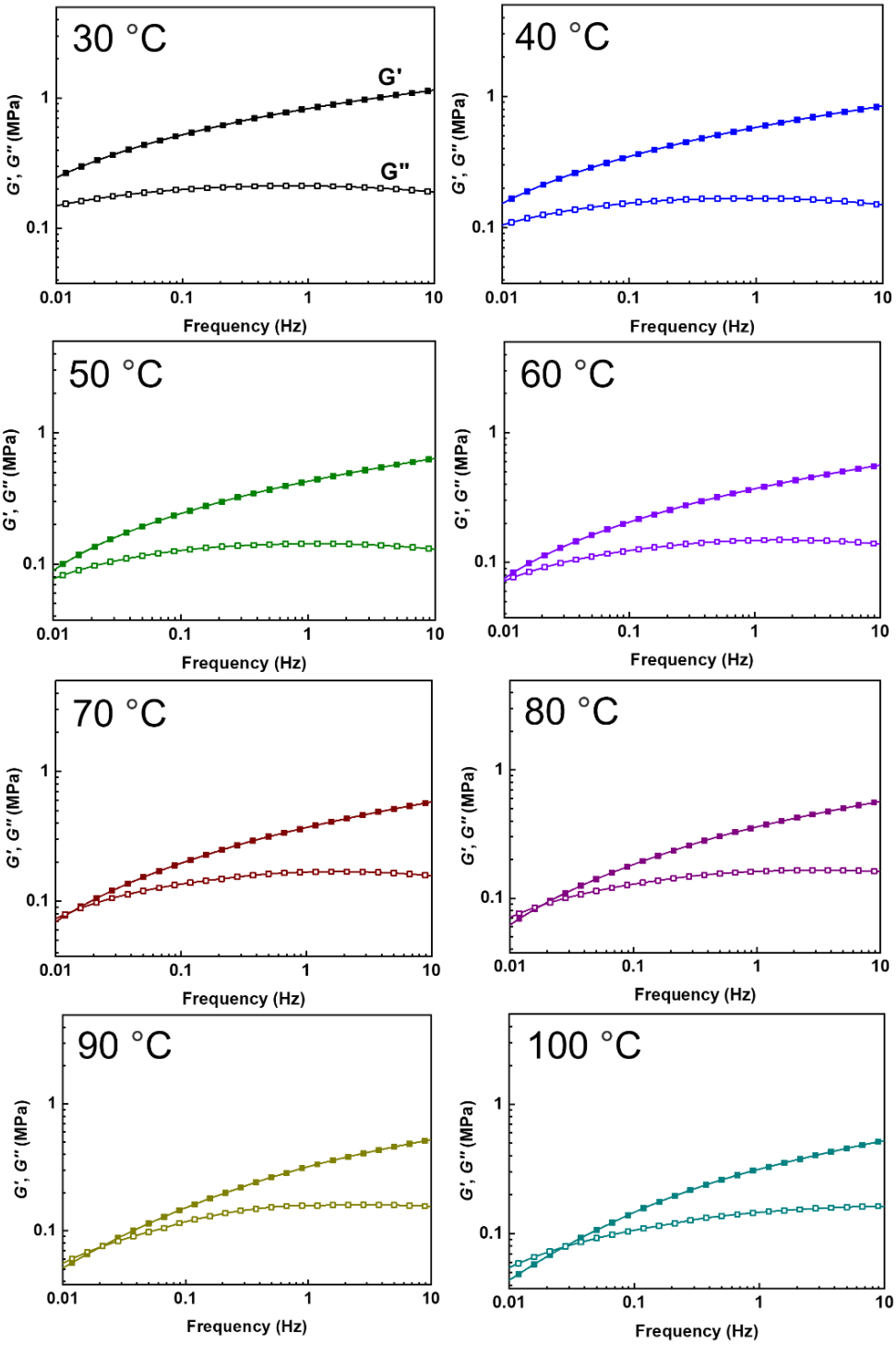

Fig. S16. Dynamic rheological data of neat PEO/LiTFSI SPE (P/Li/R2-0) in the frequency range of 0.01–10 rad s^{-1} at different temperatures. *G′*: filled squares; *G″*: unfilled squares.

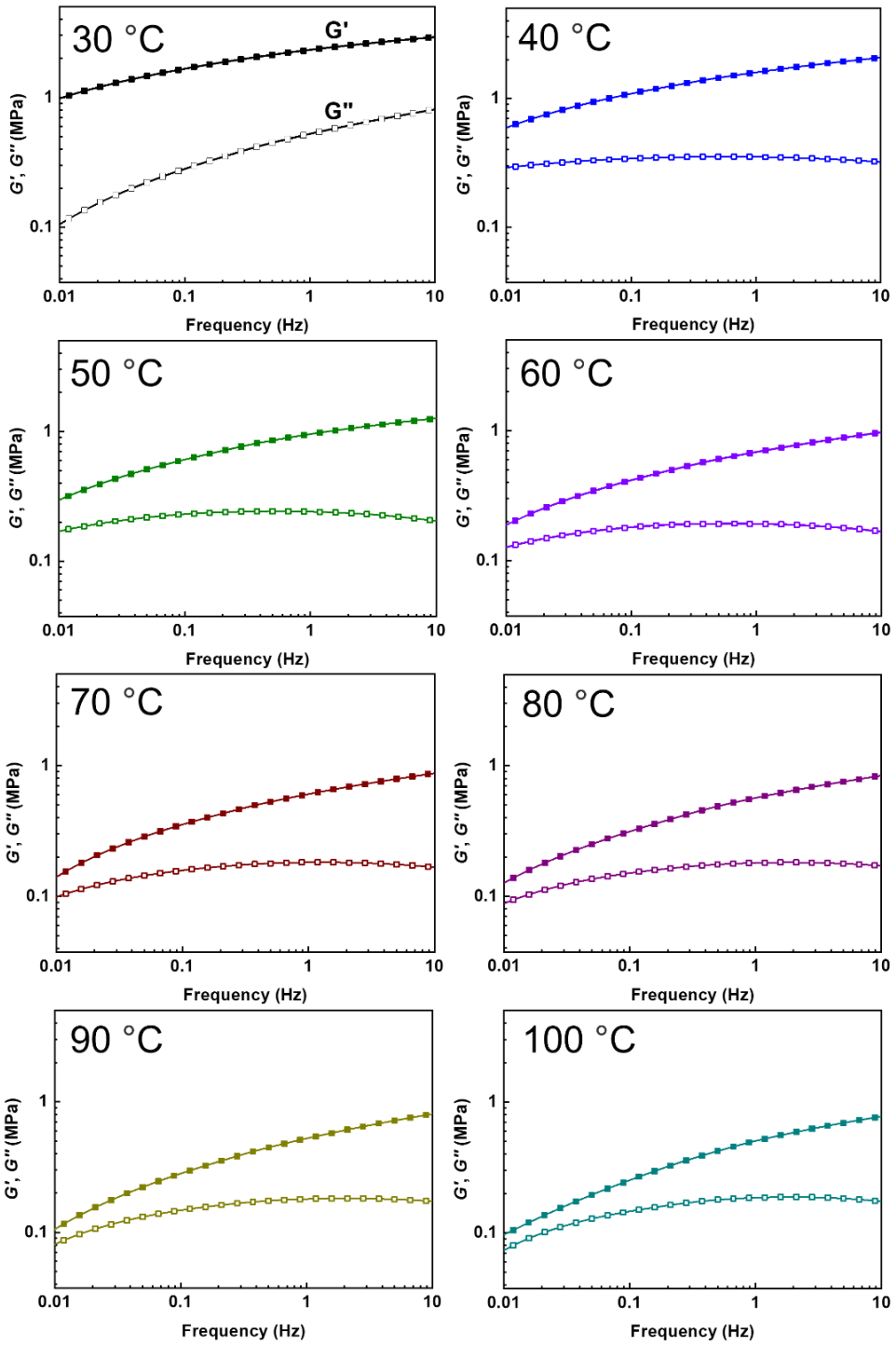

Fig. S17. Dynamic rheological data of P/Li/R2-20 SPE in the frequency range of 0.01–10 rad s^{-1} at different temperatures. *G′*: filled squares; *G″*: unfilled squares.

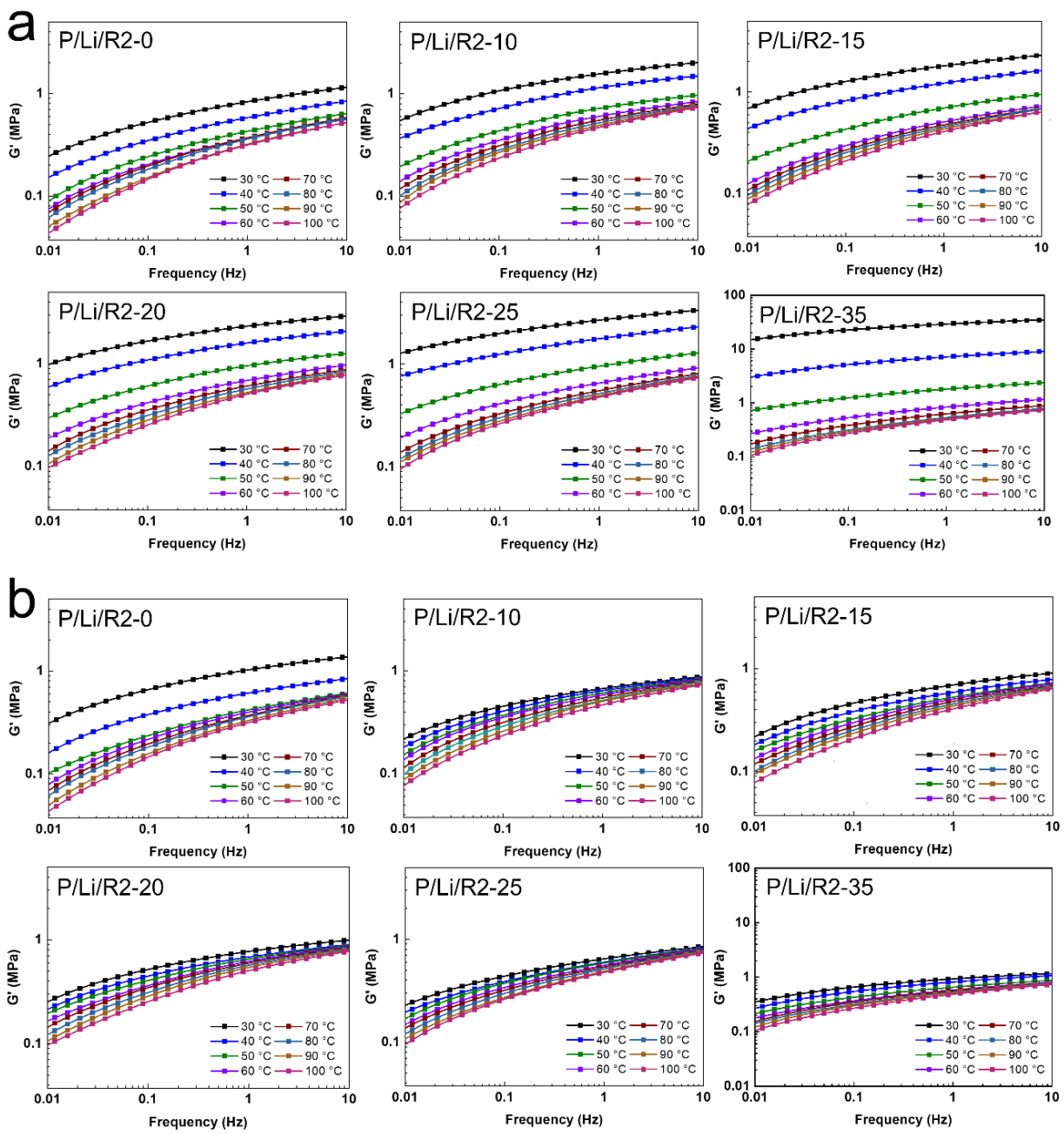

Fig. S18. Dynamic rheology curves of PEO/LiTFSI/R2 SPEs with different R2 fractions in the frequency range of 0.01–10 rad s^{-1} during (a) heating and (b) cooling.

Fig. S18 presents the dynamic rheological data of PEO/LiTFSI/R2 SPEs upon heating and cooling. As shown in **Fig. S18a**, *G′* is highly sensitive to temperature change, particularly below 50 °C, which corresponds to the transition of PEO from crystal to amorphous phases around its

melting point. Beyond this temperature, G' value gradually decreases and its slope gradually increases with increasing temperature, typical of polymer melts with a more liquid-like behavior at elevated temperature. **Fig. S18b** illustrates the change in G' of PEO/LiTFSI/R2 SPEs during cooling from 100 °C to 30 °C. For P/Li/R2-0, G' fully recovers upon cooling, as polymer chains rearrange into crystalline structures. However, for the SPEs with R2, such full recovery is not observed. For instance, the P/Li/R2-20 SPE initially shows a G' of 1 MPa at 0.01 Hz, which decreases to 0.25 MPa at 30 °C after treatment, reflecting a significant loss of mechanical strength. This reduction is attributed to the inhibition of PEO crystallization by R2, which limits chain mobility and prevents the formation of crystal structures, consistent with the DSC results (**Fig. 6b**).

S2.13. Compatibility between LiTFSI and bioengineered spider silks

The miscibility of R1 and R2 with LiTFSI is confirmed by DSC (**Fig. S19**), with a decrease in T_g observed upon LiTFSI incorporation. Therefore, the improved homogeneity and LiTFSI solubility in PEO/R2 blends are attributed to two key factors: (1) R2 reduces PEO crystallinity, increasing free volume for LiTFSI dissolution; and (2) interactions between Li^+ and the oxygen and nitrogen atoms in R2, along with coordination between $TFSI^-$ and the amides on R2, promote salt dissociation. This synergistic effect of R2 and LiTFSI results in a highly effective SPE.

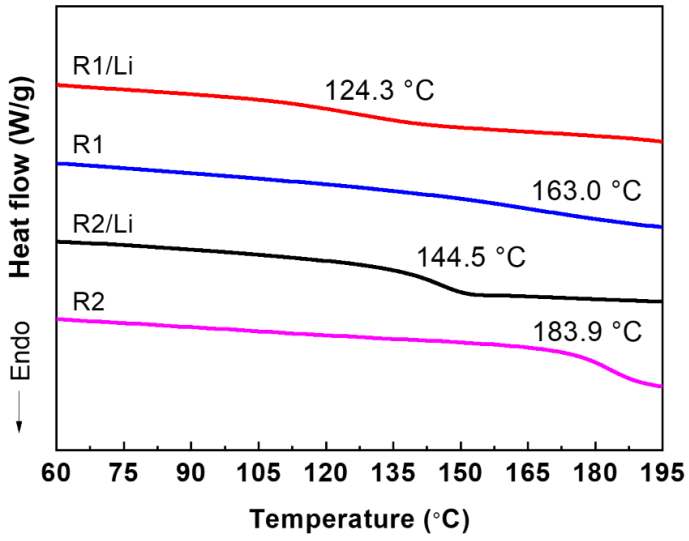

Fig. S19. DSC thermograms of R1 and R2 before and after LiTFSI incorporation.

S2.14. Thermal properties of PEO/LiTFSI/spidroin SPEs

The thermal properties of PEO-based SPEs blended with spider silk proteins were assessed through DSC analyses, as shown in **Fig. 6b** and **Fig. S20** which provide insights into the thermal behavior of the R2- and R1-reinforced SPEs, respectively. Key thermal properties, including the glass transition temperature (T_g), crystallization point (T_c), crystallization enthalpy (ΔH_c), melting point (T_m), melting enthalpy (ΔH_m), and crystallinity (χ_c) are summarized in **Table S7** and **Table S8**. Both R1 and R2 reduce PEO crystallinity and restrict crystallization, but R2 poses a stronger effect. For example, P/Li/R2-20 SPE has a lower crystallinity (16.8%) than P/Li/R1-20 (24.2%) and a higher $\Delta H_c/\Delta H_m$ value (0.89 vs. 0.84), indicating that R2 limits PEO chain mobility more effectively. This reduced crystallinity is advantageous for ionic conductivity, as ions show a greater mobility in amorphous regions. Consequently, PEO/LiTFSI/R2 SPEs are expected to exhibit higher ionic conductivity than their PEO/LiTFSI/R1 counterparts, enhancing their suitability for use in energy storage applications.

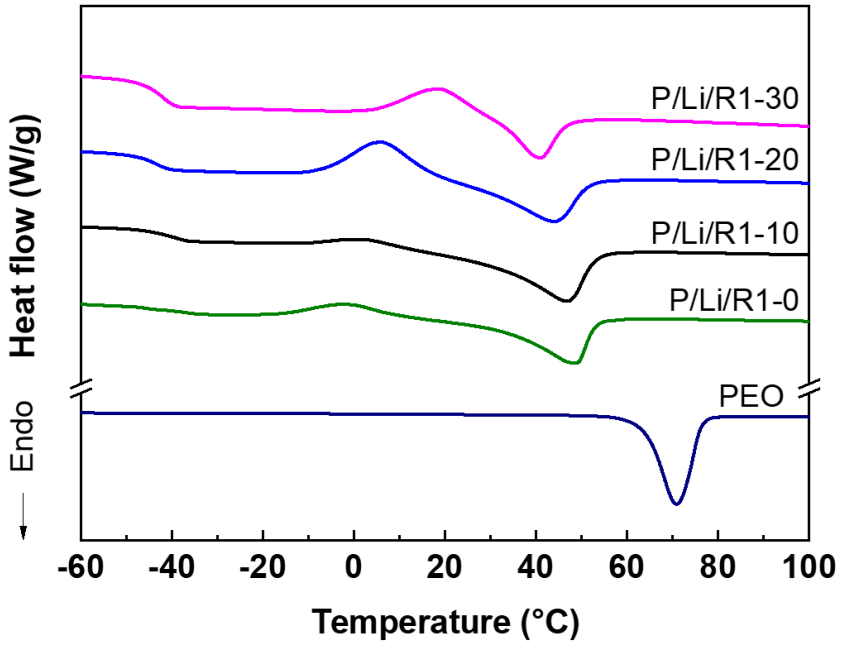

Fig. S20. DSC curves of PEO/LiTFSI/R1 SPEs with different R1 content.

Table S7. Thermal properties of PEO/LiTFSI/R2 SPEs.

Samples	T_g (°C)	T_c (°C)	ΔH_c (J/g)	T_m (°C)	ΔH_m (J/g)	χ_c (%)
P/Li/R2-35	–41.6	13.4	22.4	39.5	22.8	11.2
P/Li/R2-25	–43.0	15.6	27.4	42.8	27.5	12.6
P/Li/R2-20	–43.5	17.5	30.4	43.9	34.1	16.8
P/Li/R2-15	–44.2	12.6	36.5	45.8	40.2	19.8
P/Li/R2-10	–44.3	3.8	19.3	48.5	45.3	22.3
P/Li/R2-0	–40.5	–1.4	12.3	49.6	65.0	32.0
Pure PEO	–53.1			70.9	180.8	89.0

Table S8. Thermal properties of PEO/LiTFSI/R1 SPEs.

Samples	T_g (°C)	T_c (°C)	ΔH_c (J/g)	T_m (°C)	ΔH_m (J/g)	χ_c (%)
P/Li/R1-30	–42.3	18.6	35.9	40.6	35.7	17.6
P/Li/R1-20	–43.8	6.2	41.5	43.9	49.1	24.2
P/Li/R1-10	–41.1	1.9	10.1	46.5	60.9	30.0
P/Li/R1-0	–40.5	–1.4	12.3	49.6	65.0	32.0
Pure PEO	–53.1			70.9	180.8	89.0

S2.15. Thermal stability of PEO/LiTFSI/spidroin SPEs

TGA measurements in **Fig. S21** and **S22** demonstrate the thermal stability of PEO-based SPEs incorporated with R2 and R1. PEO/LiTFSI/R2 SPEs with varying R2 fractions display higher decomposition temperatures than pure R2 alone. The T_{d5} increases from 197 °C to 290 °C as the PEO content reaches 65% and further rises to 350 °C with a PEO fraction of 90%. The thermal stability of PEO/LiTFSI/R1 SPEs shows a similar trend, with the T_{d5} ranging from 259 °C to 356 °C with increasing PEO content. Overall, these findings suggest that PEO/LiTFSI/spidroin SPEs possess sufficient thermal stability to support their potential in high-temperature ASSLMB applications.

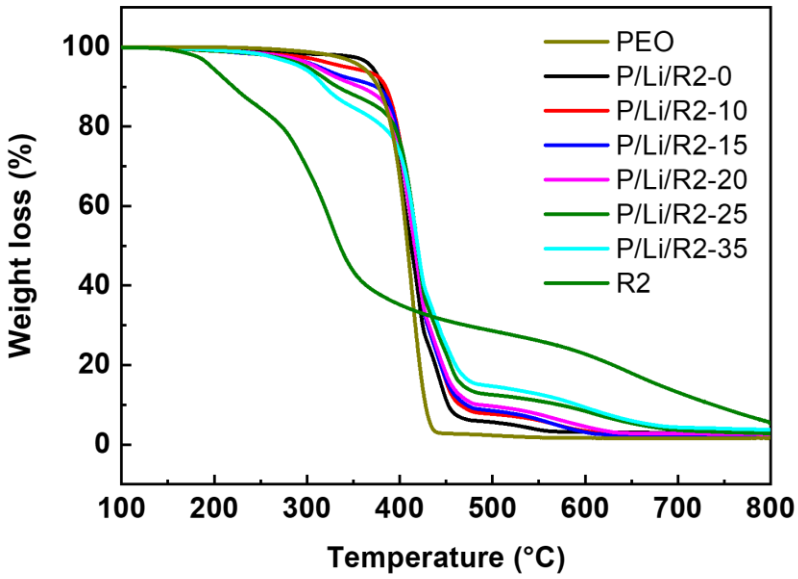

Fig. S21. TGA curves of PEO/LiTFSI/R2 SPEs with various R2 fractions.

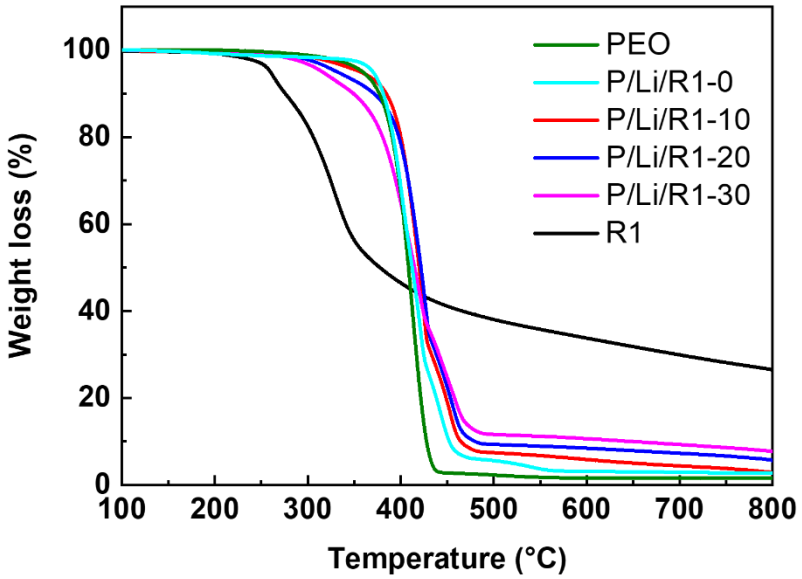

Fig. S22. TGA curves of PEO/LiTFSI/R1 SPEs with various R1 fractions.

S2.16. Modulation of crystal structures in SPEs by bioengineered spider silks

The modulation of crystal structures in SPEs by bioengineered spider silks was analyzed using WAXS. As shown in **Fig. S23** and **S24**, the incorporation of both R1 and R2 into PEO SPEs results in a notable reduction in crystallinity. This is evidenced by the diminished diffraction of the (120)

and (112) planes in the monoclinic unit cells. The ability of R1 and R2 to effectively disrupt the ordered crystal structures of PEO leads to an increase in the amorphous fraction of SPEs. This elevated amorphous content is beneficial for lithium-ion transfer, as ions predominantly navigate through amorphous regions. Thus, the integration of R1 and R2 into PEO-based SPEs enhances their ionic conductivity and supports improved performance in ASSLMBs.

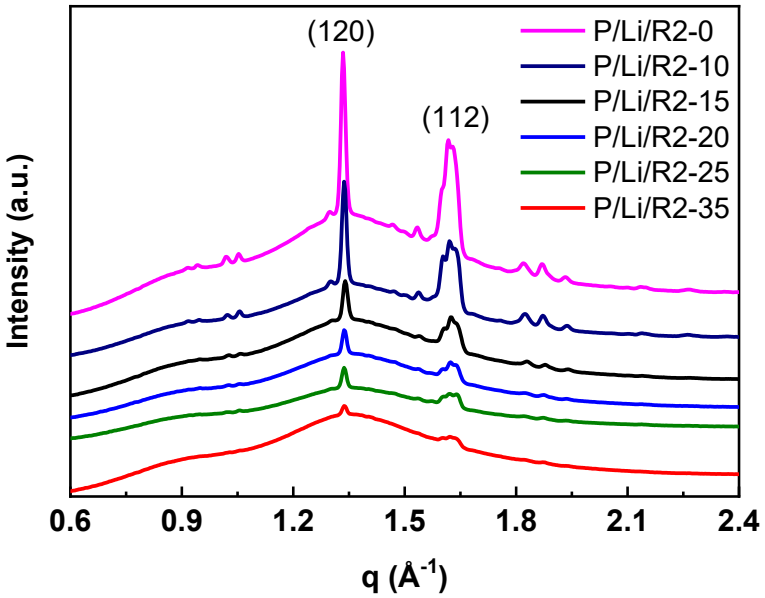

Fig. S23. WAXS profiles of PEO/LiTFSI/R2 SPEs with various R2 fractions.

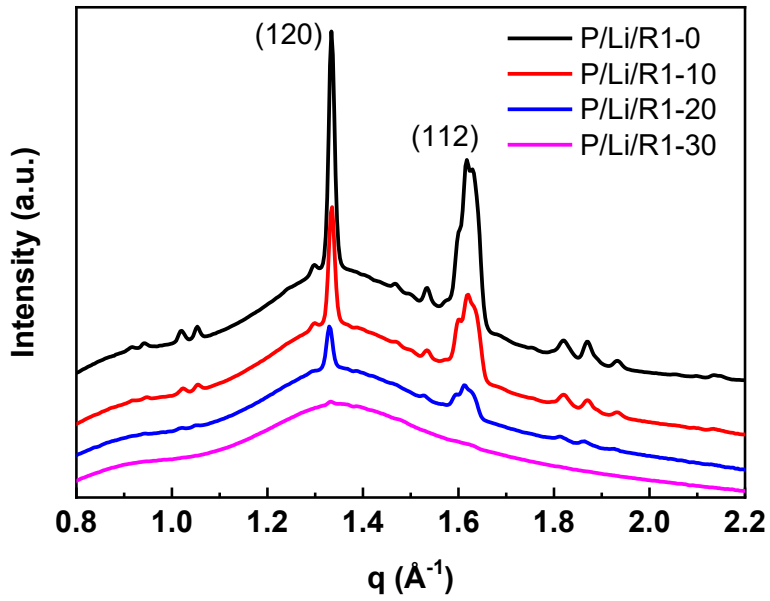

Fig. S24. WAXS profiles of PEO/LiTFSI/R1 SPEs with various R1 fractions.

Additionally, SAXS was employed to evaluate the structural evolution of PEO/LiTFSI/R2 and PEO/LiTFSI/R1 SPEs, as depicted in **Fig. S25** and **S26**. Neat PEO presents signals of crystal lamellar structure with the diffraction peaks at q values of 1:2:3 order. Upon the incorporation of LiTFSI, these discrete peaks disappear, and a broad hump appears at $q \sim 0.035$. The broad hump is caused by the form factor of the crystal lamellae of PEO. This behavior suggests that lithium ions, due to their good miscibility with PEO, significantly disrupt the order arrangement of the PEO lamellae. As the content of R2 increases in the SPEs, a slight shift of the broad hump towards higher q values is observed. A similar trend is also noted in the PEO/LiTFSI/R1 SPEs. This shift towards higher q values indicates a reduction in the size of the lamellae, suggesting further disruption in the crystal phases and enhancement of amorphous regions. These structural modifications support the enhanced electrochemical performance of the SPEs, highlighting the role of bioengineered spider silks in modulating the crystalline characteristics of PEO.

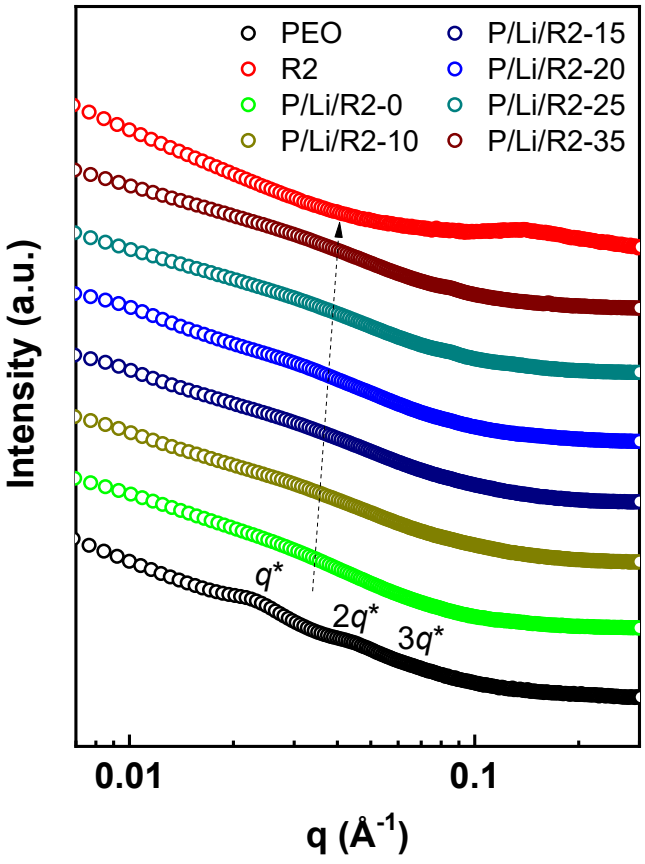

Fig. S25. SAXS profiles of PEO/LiTFSI/R2 SPEs with various R2 fractions.

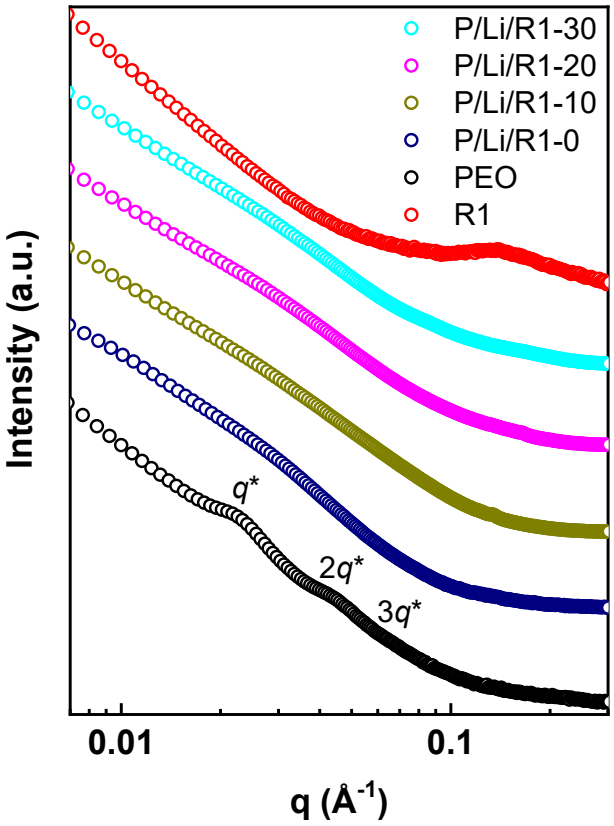

Fig. S26. SAXS profiles of PEO/LiTFSI/R1 SPEs blended with various R1 fractions.

The morphology of PEO/LiTFSI/R2 SPEs was examined using SEM and PEO. The white spots in the SEM images may be attributed to the segregation of LiTFSI particles (**Fig. S27**). LiTFSI is unable to completely dissolve in the pure PEO matrix due to the high crystallinity of PEO at room temperature. With an increase in R2 content, the samples become more homogeneous, implying a better dissolution of LiTFSI in the blends. This is attributed to the significant reduction of PEO crystallinity caused by R2, allowing more LiTFSI to dissolve in the amorphous phase. The interaction between Li^+ cations and the lone pairs of electrons on the oxygen and nitrogen atoms in spidroin also promotes the dissolution of lithium salts. The compatibility of PEO and R2, along with the enhanced solubility of lithium salts, makes PEO/LiTFSI/R2 more suitable as solid electrolytes.

The significantly decreased crystallinity of PEO can be clearly observed in POM images, as shown in **Fig. S28**. In the image of P/Li/R2-0, the spherulites of PEO (coarse bright spheres) are distributed in the matrix, with an average size of approximately 100 μm, coexisting with LiTFSI crystals (irregular bright particles) separated from PEO. The dark regions correspond to the

amorphous phase. In contrast to the large spherulites seen for neat PEO in **Fig. S9**, PEO crystallinity is reduced as lithium ions coordinate with the ether oxygen atoms on PEO. Integrating R2 into the PEO/LiTFSI matrix leads to a significant reduction in the area of the crystal phase, suggesting that R2 further hinders the crystallization of PEO. The crystalline birefringent feather nearly disappears when the R2 fraction reaches 25%. These POM images demonstrate that the incorporation of LiTFSI and R2 can effectively restrict the formation of PEO crystals, which is advantageous for lithium-ion transfer in the electrolyte.

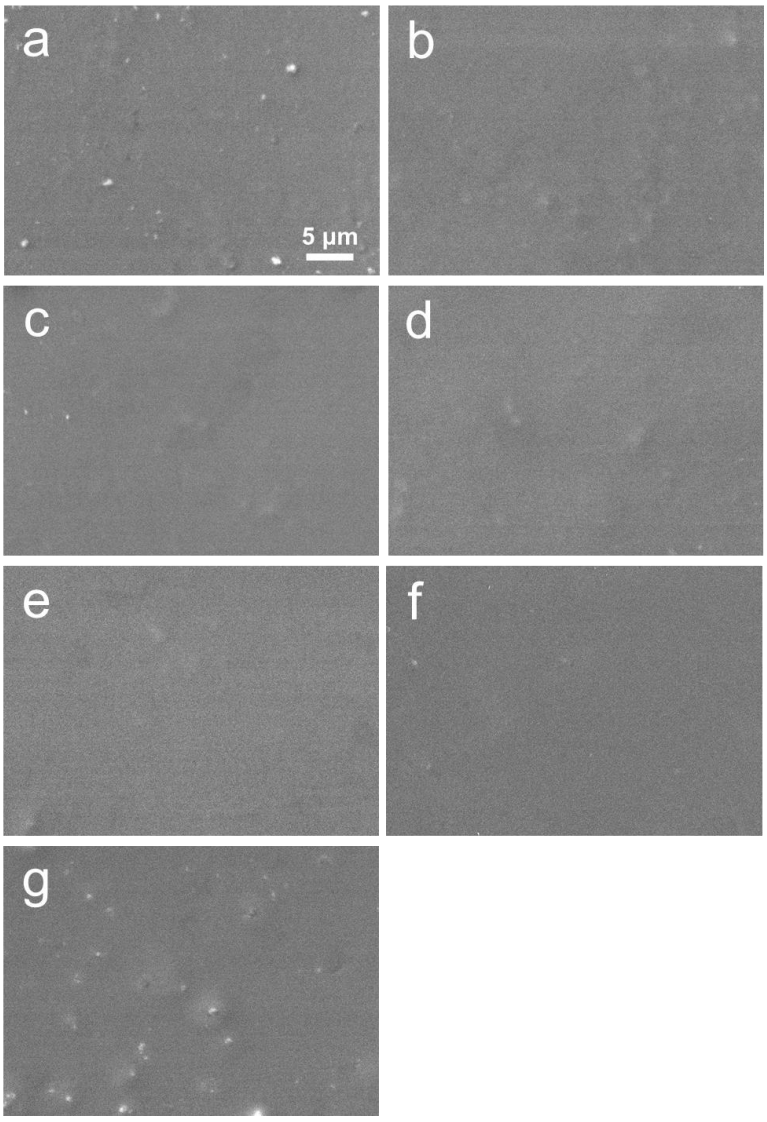

Fig. S27. SEM images of PEO/LiTFSI/R2 SPEs with different R2 fractions: (a) PEO/Li/R2-0, (b) P/Li/R2-10, (c) P/Li/R2-15, (d) P/Li/R2-20, (e) P/Li/R2-25, (f) P/Li/R2-35, and (g) neat Li/R2.

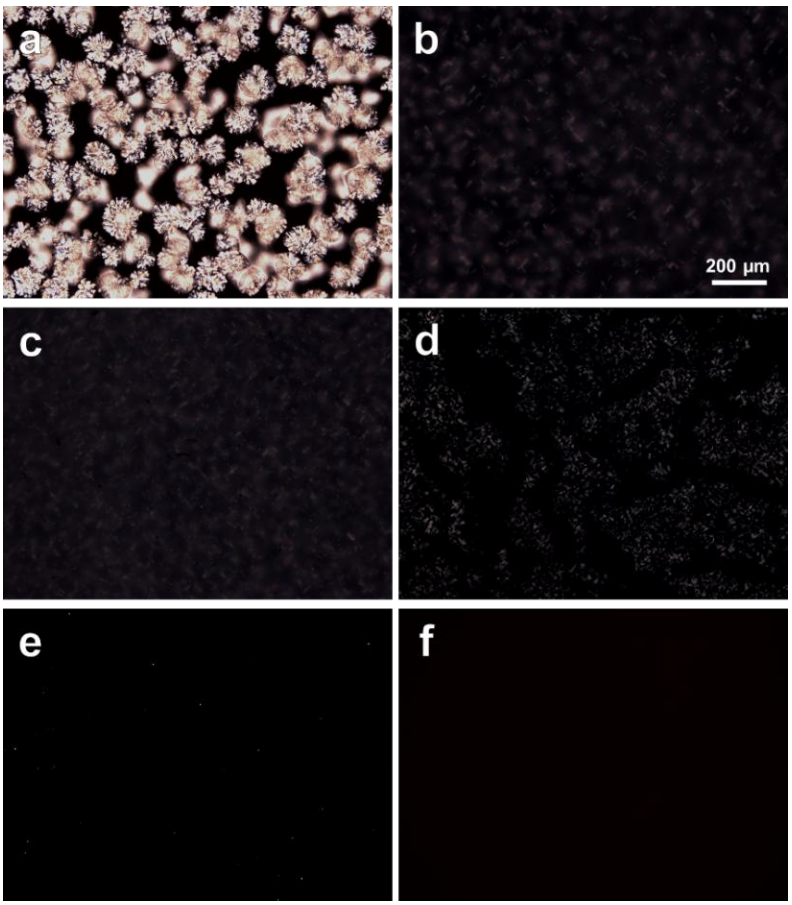

Fig. S28. POM images of PEO/LiTFSI/R2 SPEs with different R2 fractions: (a) PEO/Li/R2-0, (b) P/Li/R2-10, (c) P/Li/R2-15, (d) P/Li/R2-20, (e) P/Li/R2-25, and (f) P/Li/R2-35 SPEs.

S2.17. Electrochemical performance of PEO/LiTFSI/spidroin SPEs

The specific electrochemical impedance spectroscopy (EIS) data for the PEO/LiTFSI/R2 SPEs at different temperatures and compositions are depicted in **Fig. S29**. The ionic conductivities obtained from the EIS data are shown in **Fig. 7a**. The ionic conductivities of these electrolytes generally increase with rising temperature, as a common trend attributable to enhanced ion mobility at elevated temperatures. The addition of R2 significantly boosts the ionic conductivity of the SPEs, as anticipated from prior characterizations. Notably, the P/Li/R2-20 SPE exhibits substantially higher ionic conductivity than P/Li/R2-0 and other combinations. At 30 °C and 80 °C, the P/Li/R2-20 SPE achieves ionic conductivity values of 3.0×10^{-4} and 2.7×10^{-3} S cm^{-1}, respectively. The ionic conductivity sharply declines when the R2 ratio exceeds 25%.

Interestingly, the ionic conductivity of P/Li/R2-0 SPE displays a distinct two-stage linear behavior, with an inflection point at 50 °C, near the melting point of the SPE. Above this

temperature, PEO transforms from an elastic (semicrystalline) to a viscous (amorphous) state, thus enhancing Li^+ mobility. In contrast, R2-blended SPEs exhibit no inflection points due to the reduced crystallinity of PEO in the presence of R2. This underscores that R2 effectively enhances ionic conductivity by suppressing PEO crystallization.

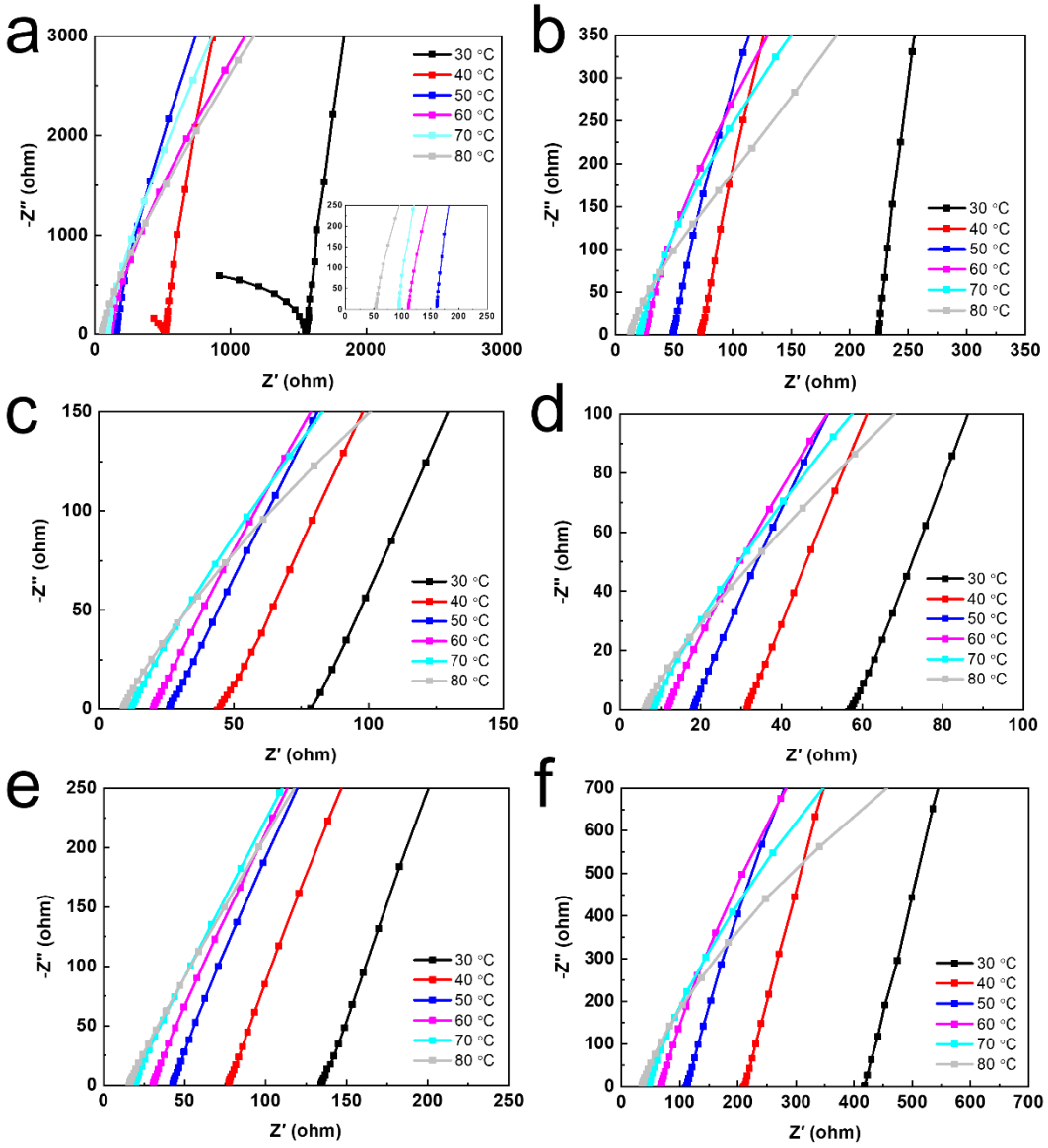

Fig. S29. Electrochemical performance of the SPEs. Nyquist plots of (a) neat PEO-based SPE (P/Li/R2-0), (b) P/Li/R2-10, (c) P/Li/R2-15, (d) P/Li/R2-20, (e) P/Li/R2-25, and (f) P/Li/R2-35 measured at various temperatures.

Table S9. Representative PEO-based blends for solid polymer electrolytes

Blends	Composition	Li salt	Ionic conductivity (S/cm)	Temp. (°C)
PEO/PMAA[30]	20/80 mol%	$LiClO_4$	1.3×10^{-5}	60
PEO/PES[31]	40/60 wt%	$LiClO_4$	3.0×10^{-5}	25
PEO/PVDF[32]	20/80 wt%	$LiClO_4$	2.6×10^{-5}	30
PEO/PEI[33]	80/20 wt%	$LiClO_4$	$\sim 10^{-4}$	RT
PEO/PET[34]	60/40 wt%	$LiClO_4$	2.0×10^{-5}	RT
PEO/PDMS[35]	70/30 wt%	$LiPF_6$	5.6×10^{-5}	30
PEO/TPU[26]	75/25 wt%	LiTFSI	5.3×10^{-4}	60
PEO/PMHS[36]	60/40 wt%	LiTFSI	2.0×10^{-2}	80
PEO/PVP[37]	75/25 wt%	$LiOOCCH_3$	2.6×10^{-6}	RT
PEO/PLA[38]	60/40 wt%	LiTFSI	$\sim 10^{-4}$	100
PEO/PPG-PEG-PPG[39]	70/30 wt%	LiTFSI	2.3×10^{-5}	RT
PEO/PVDF-HFP/PMMA[40]	50/33/17 wt%	LITFSI	1.9×10^{-4}	60
PEO/R2 (this work)	**80/20 wt%**	**LiTFSI**	**3.0×10^{-4}**	**30**

Fig. S30 displays the ionic conductivities of PEO/LiTFSI/R1 SPEs over 30 °C to 80 °C at different R1 factions. All SPEs show increased ionic conductivity with rising temperatures. PEO/LiTFSI/R1 SPEs exhibit significantly higher conductivity than the SPE without R1, among which P/Li/R1-10 SPE shows the highest ionic conductivity of 8.26×10^{-5} S cm^{-1} at 30 °C and 9.44×10^{-4} S cm^{-1} at 80 °C, compared to 8.44×10^{-6} S cm^{-1} at 30 °C and 3.90×10^{-4} S cm^{-1} at 80 °C for P/Li/R1-0. The addition of R1 can also disrupt PEO crystals, facilitating ion movement. However, PEO/LiTFSI/R1 SPEs display lower conductivity than PEO/LiTFSI/R2 SPEs (**Fig. 7a**), which demonstrates PEO/LiTFSI/R2 SPEs are a better option for the ASSLMB applications.

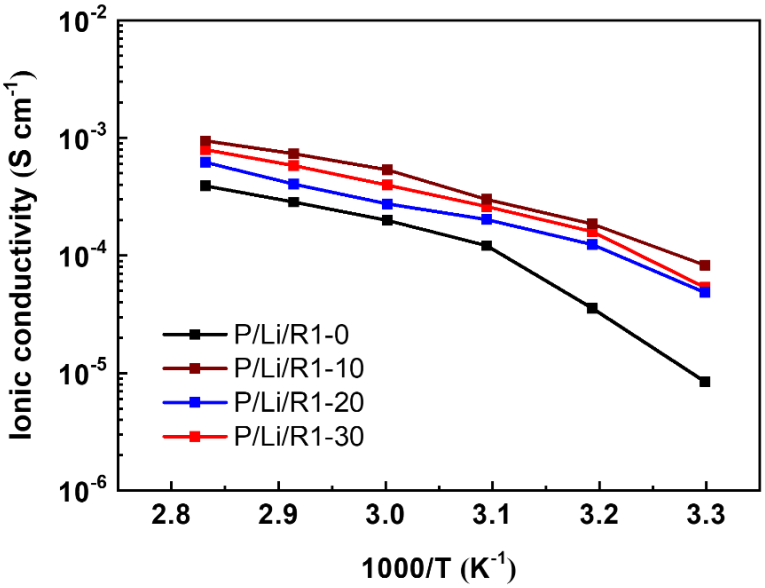

Fig. S30. Ionic conductivities of the PEO/LiTFSI/R1 SPEs at varying temperatures.

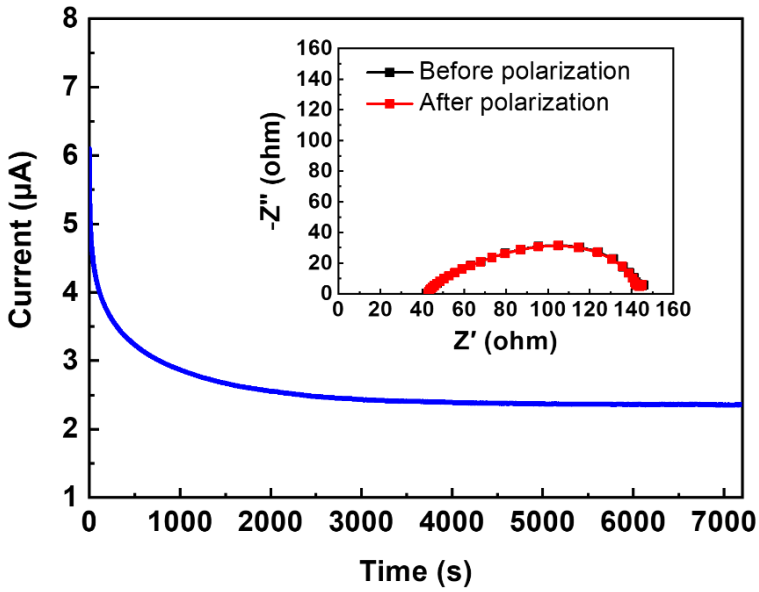

Fig. S31. Polarization curves of the Li|P/Li/R2-20|Li symmetric cell. The inset shows the electrochemical impedance spectroscopy (EIS) curves before and after polarization.

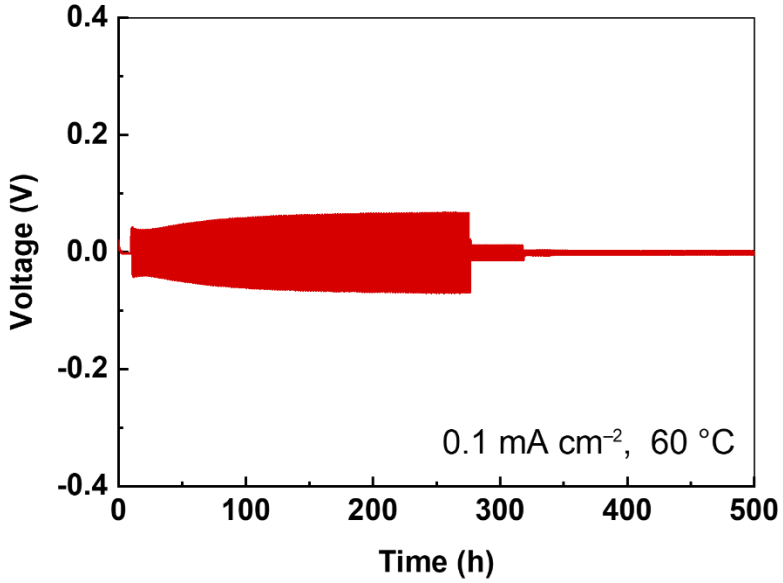

Fig. S32. Li plating/stripping test for Li|P/Li/R2-0|Li symmetric cells at 0.1 mA cm^{-2} and 60 °C. The duration of each half-cycle was 1 hour.

S3. References

1. H. C. Wu, D. N. Quan, C. Y. Tsao, Y. Liu, J. L. Terrell, X. L. Luo, J. C. Yang, G. F. Payne and W. E. Bentley, *Biotechnol. Bioeng.*, 2017, **114**, 83-95.
2. A. Pandey, T. S. Yang, T. I. Yang, W. F. Belem, N. C. Teng, I. W. Chen, C. S. Huang, A. Kareiva and J. C. Yang, *Polymers*, 2021, **13**, 2659.
3. W. C. Chen, R. C. Wang, S. K. Yu, J. L. Chen, Y. H. Kao, T. Y. Wang, P. Y. Chang, H. S. Sheu, S. C. Chen, W. R. Liu, T. Yang and H. C. Wu, *Adv. Funct. Mater.*, 2023, **33**, 2303571.
4. G. R. Strobl and M. Schneider, *J. Polym. Sci., Part B:Polym. Phys.*, 1980, **18**, 1343-1359.
5. M. S. C. Gregory P. Holland, Janelle E. Jenkins, Randolph V. Lewis, and Jeffery L. Yarger, *J. Am. Chem. Soc.*, 2008, **130**, 9871-9877.
6. M. Hronska, J. D. van Beek, P. T. F. Williamson, F. Vollrath and B. H. Meier, *Biomacromolecules*, 2004, **5**, 834–839.
7. J. E. J. Melinda S. Creager, Leigh A. Thagard-Yeaman, Amanda E. Brooks, Justin A. Jones, Randolph V. Lewis, Gregory P. Holland, and Jeffery L. Yarger, *Biomacromolecules*, 2010, **11**, 2039–2043.
8. X. Shi, G. P. Holland and J. L. Yarger, *Biomacromolecules*, 2015, **16**, 852-859.
9. T. Asakura and J. Yao, *Protein Sci.*, 2002, **11**, 2706-2713.
10. R. Witter, U. Sternberg and A. S. Ulrich, *J. Am. Chem. Soc.*, 2006, **128**, 2236–2243.
11. L. Dambies, C. Guimon, S. Yiacoumi and E. Guibal, *Colloids Surf., A*, 2001, **177**, 203-214.
12. T. Valisälmi, N. Roas-Escalona, K. Meinander, P. Mohammadi and M. B. Linder, *Langmuir*, 2023, **39**, 4370-4381.
13. P. Papadopoulos, J. Solter and F. Kremer, *Eur. Phys. J. E:Soft Matter Biol. Phys.*, 2007, **24**, 193-199.

14. A. Heidebrecht, L. Eisoldt, J. Diehl, A. Schmidt, M. Geffers, G. Lang and T. Scheibel, *Adv. Mater.*, 2015, **27**, 2189-2194.
15. M. A. Koperska, D. Pawcenis, J. Bagniuk, M. M. Zaitz, M. Missori, T. Łojewski and J. Łojewska, *Polym. Degrad. Stab.*, 2014, **105**, 185-196.
16. F. Vilaplana, J. Nilsson, D. V. Sommer and S. Karlsson, *Anal. Bioanal. Chem.*, 2015, **407**, 1433-1449.
17. M. A. de Moraes, C. R. Albrecht Mahl, M. Ferreira Silva and M. M. Beppu, *J. Appl. Polym. Sci.*, 2015, **132**, 41802.
18. A. Barth, *Biochim. Biophys. Acta*, 2007, **1767**, 1073-1101.
19. F. Paquet-Mercier, T. Lefèvre, M. Auger and M. Pézolet, *Soft Matter*, 2013, **9**, 208-215.
20. D. Wilson, R. Valluzzi and D. Kaplan, *Biophys. J.*, 2000, **78**, 2690-2701.
21. N. Du, X. Y. Liu, J. Narayanan, L. Li, M. L. Lim and D. Li, *Biophys. J.*, 2006, **91**, 4528-4535.
22. J. O. Warwicker, *J. Mol. Biol.*, 1960, **2**, 350-362.
23. J. O. Warwicker, *Acta Crystallogr.*, 1954, **7**, 565-573.
24. M. M. Christian Riekel, and Fritz Vollrath, *Macromolecules*, 1999, **32**, 4464-4466.
25. M.-E. Rousseau, D. H. Cruz, M. M. West, A. P. Hitchcock and M. Pézolet, *J. Am. Chem. Soc.*, 2007, **129**, 3897–3905.
26. C. Tao, M.-H. Gao, B.-H. Yin, B. Li, Y.-P. Huang, G. Xu and J.-J. Bao, *Electrochim. Acta*, 2017, **257**, 31-39.
27. M. Dissanayake and R. Frech, *Macromolecules*, 1995, **28**, 5312-5319.
28. T. Inoue, M. Matsuda, Y. Nibu, Y. Misono and M. Suzuki, *Langmuir*, 2001, **17**, 1833-1840.
29. Y. Su, J. Wang and H. Liu, *J. Phys. Chem. B*, 2002, **106**, 11823-11828.
30. E. Tsuchida, H. Ohno, K. Tsunemi and N. Kobayashi, *Solid State Ionics*, 1983, **11**, 227-233.
31. D. W. Kim, J. K. Park and H. W. Rhee, *Solid State Ionics*, 1996, **83**, 49-56.
32. M. M. E. Jacob, S. R. S. Prabaharan and S. Radhakrishna, *Solid State Ionics*, 1997, **104**, 267-276.
33. R. Tanaka, M. Sakurai, H. Sekiguchi, H. Mori, T. Murayama and T. Ooyama, *Electrochim. Acta*, 2001, **46**, 1709-1715.
34. J. S. Oh, S. H. Kim, Y. Kang and D. W. Kim, *J. Power Sources*, 2006, **163**, 229-233.
35. A. Das, A. K. Thakur and K. Kumar, *Ionics*, 2013, **19**, 1811-1823.
36. Y. J. Li, C. Y. Fan, J. P. Zhang and X. L. Wu, *Dalton Trans.*, 2018, **47**, 14932-14937.
37. K. Sundaramahalingam, M. Muthuvinayagam and N. Nallamuthu, *Polym. Sci., Ser. A*, 2019, **61**, 565-576.
38. J. L. Olmedo-Martínez, L. Porcarelli, G. Guzmán-González, I. Calafel, M. Forsyth, D. Mecerreyes and A. J. Müller, *ACS Appl. Polym. Mater.*, 2021, **3**, 6326-6337.
39. R. Y. Li, H. M. Hua, Y. J. Zeng, J. Yang, Z. Q. Chen, P. Zhang and J. B. Zhao, *J. Energy Chem.*, 2022, **64**, 395-403.
40. J. S. Wang, Y. Q. Zhang, Z. X. Chen, S. Fan, Q. H. Zhang, Y. Zhang, T. D. Zhang, C. H. Zhang and Q. G. Chi, *Chem. Eng. J.*, 2024, **492**, 152222.